Engineering Structures 245 (2021) 112908

Contents lists available at ScienceDirect

Engineering Structures

journal homepage: www.elsevier.com/locate/engstruct

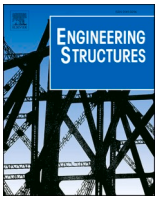

Finite-element-based concept to predict stiffness, strength, and failure of wood composite I-joist beams under various loads and climatic conditions

Maximilian Autengruber [a,*], Markus Lukacevic [a], Gregor Wenighofer [b], Raimund Mauritz [b], Josef Füssl [a]

[a] Institute for Mechanics of Materials and Structures, TU Wien, Karlsplatz 13, Vienna 1040, Austria
[b] Doka GmbH, Josef Umdasch Platz 1, Amstetten 3300, Austria

ARTICLE INFO

Keywords:
Coupled moisture transport
Cracks
Failure
Multisurface failure criterion
Wood composite

ABSTRACT

Formwork support constructions are an indispensable part of almost all reinforced concrete structures. The main supporting system usually consists of wood-based composites, where solid timber, plywood and, more recently, aluminum profiles are combined to form I-beams. These beams have to go through a very complex test program, to ensure that they withstand all mechanical and moisture-related stresses during their service life. To better understand the mechanisms leading to mechanical failure as well as to support a targeted optimization of new cross section types, we developed a finite-element-based simulation concept. Moisture-related effects occurring during the service life are considered with an advanced moisture transport model and a multisurface failure criterion is implemented for modeling the plastic and brittle failure mechanisms in wood, resulting in a very good prediction of stiffness values, load-carrying capacities and failure behavior of the experimentally investigated beams. The performance of the modeling approach is shown by simulation of three different experiments, representing different mechanical loading situations at three different moisture levels.

1. Introduction

The development of new wood products is a challenging task due to the naturally grown structure of wood and its moisture-dependent material properties, especially when different wood and wood-based materials are combined in one beam, as is the case with wood composite beams with an I-joist shape for formwork.

The cross sections of such beams are defined on the basis of the specifications from the standard EN 13377 [1] and divided into certain classes. The flange of the investigated beams of P20 class is made of spruce solid timber and the web of a particle board. This standard-type beam is referred to as *H20 top P* while the newly developed *I tec pro* beam incorporates an aluminum profile in the region of the flange. In addition to the geometric specifications also experimental setups are defined in the standard EN 13377 to determine structural parameters of the developed beams in bending, shear and bearing resistance tests. These tests have to be perfomed at a moisture content (MC) of 12±2%.

About 46% of damage cases of large span timber constructions can be related to moisture events according to [2]. When designing wooden beams used in formwork for concrete constructions, changing environmental conditions during loading as well as storing play a role. Since these beams are re-used on different construction sites, they are also exposed to different climate conditions during their service life. To reflect this in the experimental program, the resistance tests are performed in two additional moisture conditions, resulting in the following three states:

- *dry:* at an MC for spruce of 12% and 293.15 K,
- *moist:* after 3 days of exposure to 100% relative humidity at 293.15 K and
- *wet:* after 60 days of exposure to 100% relative humidity at 293.15 K.

Various concepts exist for modeling moisture transport in wood. The most advanced so far is the multi-Fickian transport model as described in [3–8], which is especially able to appropriately describe high moisture content gradients that occur in samples with a thickness of more than a few millimeters and relative humidities of more than 65% according to [9]. However, this model has so far only been applied to solid wood, but not to particle board. Diffusion coefficients of particle boards were investigated in [10,11]. In contrast to solid wood, the directional

* Corresponding author.
E-mail address: maximilian.autengruber@tuwien.ac.at (M. Autengruber).

https://doi.org/10.1016/j.engstruct.2021.112908
Received 29 December 2020; Received in revised form 23 June 2021; Accepted 24 July 2021
Available online 13 August 2021

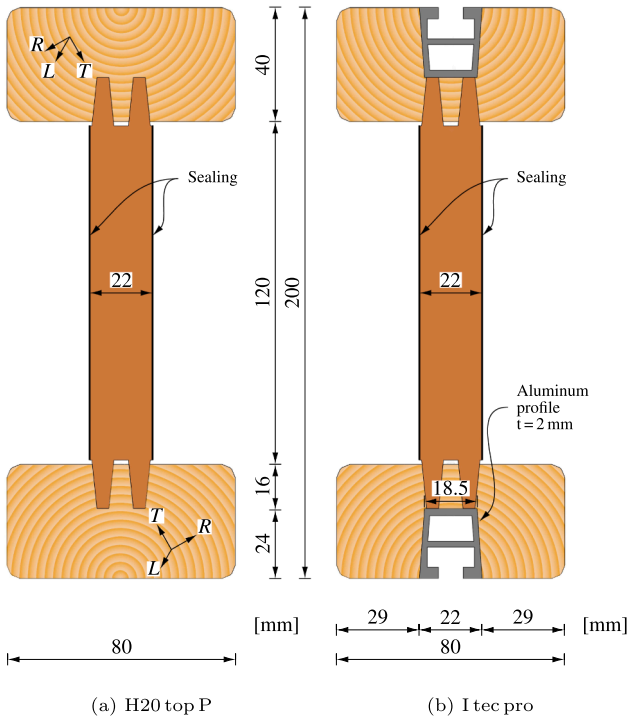

(a) H20 top P (b) I tec pro

Fig. 1. Investigated cross sections of P20 class. The flanges with a cross section of 4x8 cm are made of solid timber with the pith located in the middle of the top and bottom edge, respectively, and the web is made of a 22 mm thick special type particle board, which is sealed. In case of the *I tec pro* an aluminum profile is placed in the flanges as can be seen in (b).

behavior of the particle board is different, as the two characteristic directions are in-plane and out-of-plane.

After the beams are conditioned to the required moisture level, the resistance tests according to EN 13377 are performed. Depending on the type of resistance test, different mechanisms lead to failure. In case of the bending resistance test the tensile strength of spruce in longitudinal direction is the most significant contribution. In the literature, failure of spruce is most accurately described with a complex multisurface criterion based on [12–16], which was also used in [17] to determine crack patterns in wooden cross sections under changing climate loading, leading to brittle or ductile failure modes. In bearing and shear resistance tests, the special type particle board plays a significant role. The failure of such boards is investigated for instance in [18]. For the aluminum profile, the von Mises plasticity is generally used.

The main objective of this work is to present an advanced simulation concept for predicting the stiffness and strength of wood composite I-joist beams at different moisture states, and the same time the validation of this tool on the basis of several experiments. For this purpose, after defining the final material properties and definitions as well as describing the experimental setups in Section 2, the determination of the unknown parameters by means of a sensitivity analyses and a parameter studies are described, since not all mechanical material parameters are directly available from experiments (e.g. coefficients of friction, elasticity tensors of the particle board and load transmission construction), in Section 3.1. This is followed by the resulting moisture fields after the exposure to wet conditions, which are presented in Section 3.2. With these determined, the simulated resistance tests are then outlined for the two beams in different moisture states and compared with the corresponding experimental results in Section 3.3–3.5.

2. Materials and methods

Moisture leads to dimensional changes of the wooden parts and also variations in the material properties, which must be taken into account when determining the stiffness and maximum load-carrying capacity of the beams in different moisture conditions. Therefore, a hygrothermal multi-Fickian transport model is evaluated first and the resulting moisture and temperature fields are then applied in a second mechanical analysis, where also the external loads according to EN 13377 are applied, to determine the load–displacement behavior and the maximum load-carrying capacity.

2.1. Cross sections

In this work two different types of beams of the P20 class according to EN 13377 with a total height of 20 cm, a flange width of 8 cm and flange height of 4 cm are presented. The *H20 top P* cross section in Fig. 1a consists of two flanges made of spruce solid timber and a web made of a 22 mm thick special type particle board. The newly developed *I tec pro* beam in Fig. 1b has two additional aluminum profiles placed in the flanges to increase the strength while the remaining geometry is similar to the *H20 top P*.

2.2. Moisture transport simulations

For conditions below the fiber saturation point (FSP), moisture transport in wood can be modeled with the multi-Fickian theory as described in [3,5,7–9,19], where two diffusion processes, one for water vapor in the lumen of the cell and one for bound water in the cell wall, act in parallel and are coupled via the sorption rate. An energy conservation equation completes the system of equations, considering the enthalpy changes due to the transport processes and also the thermal conduction process. The model is based on the theory of drying in porous media from [20], where volume averaging of the parameters was used. While the bound water concentration degree of freedom (c_b) and the sorption rate ($\dot{c}_{bv}$) are defined over the whole representative volume element (RVE), the water vapor concentration degree of freedom (c_v) refers only to the lumen part of the volume, which is defined with the volume proportion f_{lum}. The third degree of freedom is the temperature T, also defined over the whole RVE. The moisture content (MC) is defined as the bound water concentration by the dry density of wood (c_b/ρ_d).

In the present paper, the model of [8,17] was used, without the free water conservation equation since no free water is present, resulting in the following set of governing equations:

Conservation of bound water concentration:

$$\frac{\partial c_b}{\partial t} = \frac{\partial}{\partial \boldsymbol{x}} \cdot \boldsymbol{D_b} \cdot \frac{\partial c_b}{\partial \boldsymbol{x}} + \frac{\partial}{\partial \boldsymbol{x}} \cdot \boldsymbol{D_{bT}} \cdot \frac{\partial T}{\partial \boldsymbol{x}} + \dot{c}_{bv} \tag{1}$$

Conservation of water vapor concentration:

$$\frac{\partial c_v f_{lum}}{\partial t} = \frac{\partial}{\partial \boldsymbol{x}} \cdot \boldsymbol{D_v} \cdot \frac{\partial c_v}{\partial \boldsymbol{x}} f_{lum} - \dot{c}_{bv} \tag{2}$$

Conservation of energy:

$$\begin{aligned} \frac{\partial \rho\, h}{\partial t} = &+ \frac{\partial}{\partial \boldsymbol{x}} \cdot \boldsymbol{K} \cdot \frac{\partial T}{\partial \boldsymbol{x}} \\ &+ \frac{\partial}{\partial \boldsymbol{x}} \cdot \boldsymbol{D_b} \cdot \frac{\partial c_b}{\partial \boldsymbol{x}} \bar{h}_b + \frac{\partial}{\partial \boldsymbol{x}} \cdot \boldsymbol{D_{bT}} \cdot \frac{\partial T}{\partial \boldsymbol{x}} \bar{h}_b \; (h_v - h_b) \\ &+ \frac{\partial}{\partial \boldsymbol{x}} \cdot \boldsymbol{D_v} \cdot \frac{\partial c_v}{\partial \boldsymbol{x}} h_v f_{lum} \\ &+ \dot{c}_{bv} \end{aligned} \tag{3}$$

Where the left hand side shows the accumulation expression, which accounts for the change of the concentration/energy over time ∂t, and the right hand side the diffusion processes with transport tensors for bound water $\boldsymbol{D_b}$ and water vapor $\boldsymbol{D_v}$ as well as the phase change between the two states of water, which is denoted with the sorption rate $\dot{c}_{bv}$. In Eq. (3), the thermal conduction $\boldsymbol{K}$ is considered together with the

Table 1
Entries for elasticity tensor $\boldsymbol{C}$ at 12% MC and 293.15 K in MPa for a dry density of 405 kg m^{-3}.

C_{LLLL}	C_{RRRR}	C_{TTTT}	C_{LLRR}	C_{RRTT}	C_{TTLL}	C_{LRLR}	C_{LTLT}	C_{RTRT}
12205	799	532	274	376	216	567	578	73.2

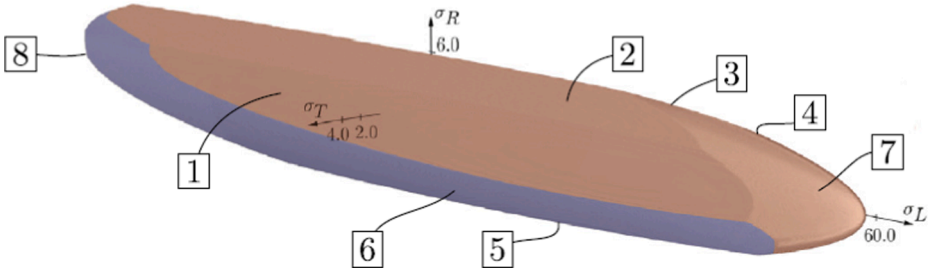

Fig. 2. Multisurface failure criterion shown in the σ_L–σ_R–σ_T-space from [14]. The numbers denote the fracture surfaces. Brittle fracture is defined by surfaces 1–3 and 7 and ductile failure by 4–6 and 8.

Table 2
Entries for the elasticity tensor C and yield strength for the particle board in MPa. Directions 1 and 2 are in-plane.

Conditions	C_{1111}	C_{1122}	C_{2222}	C_{1133}	C_{2233}	C_{3333}	C_{1212}	C_{1313}	C_{2323}	Yield strength
dry	7597	5797	7597	1863	1863	668	901	47.7	47.7	32.5
moist/wet	3039	2319	3038.9	745	745	267	360	19.1	19.1	23.7/14.6

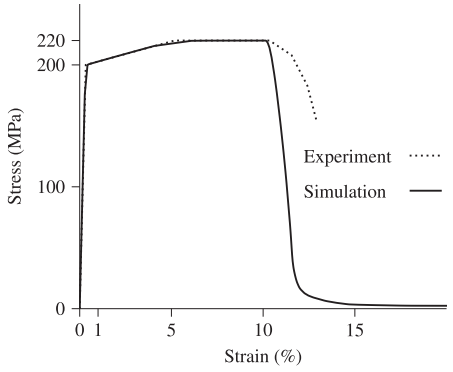

Fig. 3. Stress–strain relationship of a uniaxial tensile test of an AW 6060 T66 aluminum specimen used for the profile. in the *I tec pro* beam. Calibrated simulation results shown in comparison to the experimental results.

Table 3
Definition of the ductile material behavior of aluminum. Failure is considered on the basis of a von Mises yield criterion including a yield plateau and subsequent softening.

Yield stress (MPa)	Plastic strain (-)
200	0
220	0.0484
220	0.1500
1	0.4000

enthalpy changes due to the transport processes, which are considered with $\overline{h}_b$ as the averaged enthalpy of bound water and h_v as the specific enthalpy of water vapor. The phase change, based on the sorption rate, is considered with the enthalpy difference between h_v and h_b, where h_b is the specific enthalpy of bound water. The constitutive equations are given in Appendix A.

The system of Eqs. (1)–(3) is implemented with a user element subroutine in the finite element software *Abaqus* [21] with brick-type elements using linear interpolation functions for the discretization and solved by using the modified Newton method, according to [8].

2.2.1. *Material properties for moisture transport*

As the User Element Subroutine was used in the whole cross sections, the moisture and temperature transport are modeled with the same multi-Fickian transport model, as previously described, in all three materials. Thus, the special type particle board and also the aluminum profile have to be used with properties fitting into this model as described in the following paragraphs.

2.2.1.1. Solid timber (spruce). The material parameters for spruce are defined according to [17], but with a dry density of 405 kg m^{-3}, corresponding to the mean value of the spruce samples and given in Table A.1 and A.2 in Appendix A. A cylindrical-orthotropic material orientation was defined in each integration point, depending on the pith location in the lower and upper flange, by means of a user subroutine. A sorption hysteresis was also included to define the sorption rate $\dot{c}_{bv}$ under the isothermal experimental conditions.

2.2.1.2. Particle board. To model the moisture transport in the particle board, the following similarities and differences to solid timber are taken into account:

- The cell walls of the wood particles of the board have the same properties as in solid timber.
- In contrast, both the glue and the compaction during the manufacturing process reduce the diffusivities in the lumen compared to solid timber.

Considering these statements, and because this allows the same user element to be used throughout the entire cross section, we also use a multi-Fickian model for the moisture transport in this material. However, to the authors' knowledge, no transport parameters exist to describe moisture transport within the particle board in terms of such a

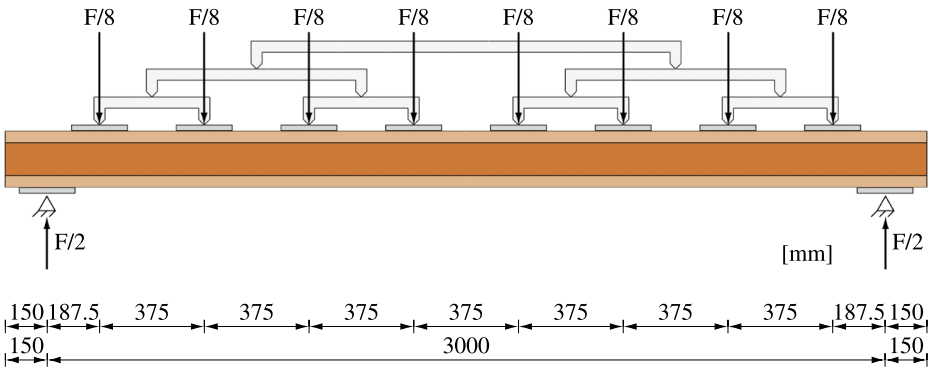

Fig. 4. Test for bending resistance according to EN 13377. The 3.30 m long beam is loaded with eight single forces and supported at two locations at the end of the beam.

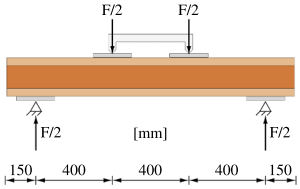

Fig. 5. Test for shear resistance according to EN 13377. The 1.50 m long beam is loaded with two single forces and supported at two locations at the end of the beam.

model and, thus, the same diffusivities are assumed for transport in the cell walls of the particles as for solid timber, while the value for vapor diffusivity is reduced as described in the following:

For the moisture diffusivities, a value for μ of 20 for wet particle boards and 50 for dry ones is given in [22]. Since the standard does not distinguish between the two water phases, it is assumed, that the dry value represents the water vapor diffusion property and the other part of the moisture transport process is considered with bound water diffusion. The reduction tensor for water vapor diffusion $\boldsymbol{\xi}$ is determined based on the reciprocal value of μ, which results in 0.02 for the out-of-plane direction. Based on [10] the in-plane diffusivity of particle boards is about 15 times larger than the one in out-of-plane direction, thus, the in-plane value is set to 0.3.

For the bound water diffusivity, the coefficients were scaled from solid timber of the previous section. In [22], the same μ values are given for a particle board and solid timber and, thus, for the diffusivity in the out-of-plane direction the value from the radial direction (which is equal to the tangential direction) of solid timber was chosen. However, for the longitudinal direction, the bound water transport in solid timber is 2.5 times larger than in the other directions. For the water vapor diffusivity, this factor is about 20 in case of solid timber (see on Table A.2), when comparing the longitudinal and tangential directions, and 15, as previously mentioned, for the particle board. Thus, the factor for the longitudinal component of the bound water diffusivity is set to 1.875.

This assumption for the bound water transport, where the glue has no influence, should lead to higher moisture contents and, thus, be on the safe side regarding deformations and subsequent failure mechanisms. The consequences of this assumption on the simulation results will be addressed in the discussion section of the paper.

A comparison of the diffusivities for the different materials and phases of water is shown in Table A.2 in Appendix A. The specific heat capacity is set to 1700 J kg^{-1} K^{-1} according to [22] and the thermal conductivity is interpolated from the data given in [22] with 0.167 W m^{-1} K^{-1}.

The sorption process was modeled with the same hysteresis model as used for solid timber, hence the particle board is based on solid timber particles, but the isotherms were adjusted to the dry density of the particle board by scaling with the relation of the dry densities ($\rho_{d,sp}/\rho_{d,pb}$). As the particles consist of the same solid wood material, also the specific and averaged bound water enthalpy expressions from solid timber were used for the particle board.

The special type particle board is sealed, as shown in Fig. 1, with a material similar to bitumen paper, which has an s_d-value of 2 m according to [22].

2.2.1.3. Aluminum. The multi-Fickian model was also used for the aluminum profile, but with the diffusion coefficients set to zero, leaving only thermal conduction active in this material. The density of aluminum is set to 2700 kg m^{-3}, the heat capacity to 897 J kg^{-1} K^{-1} and the thermal conductivity to 235 W m^{-1} K^{-1}.

2.2.2. Glue lines and interaction between parts

The components of the cross sections are combined with an adhesive of type 1C-PUR, which has a higher diffusion resistance than e.g. MUF.

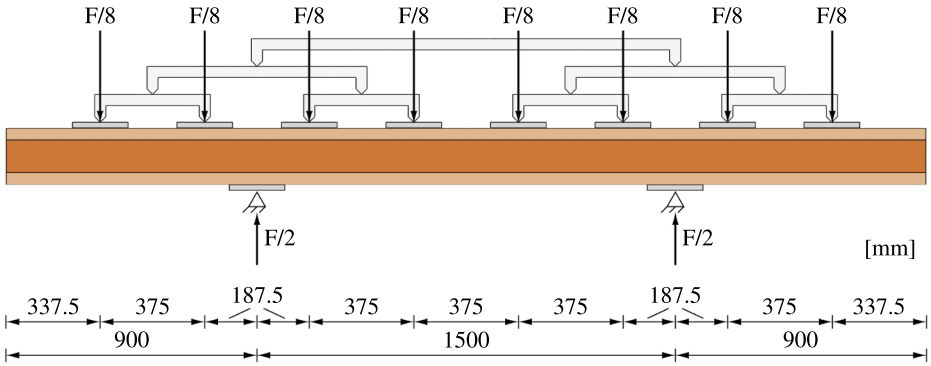

Fig. 6. Test for bearing resistance according to EN 13377. The 3.30 m long beam is loaded with eight single forces and supported at two locations of the beam.

Table 4
Variation of parameters and their influence on beam stiffness in case of *I tec pro* relative to a reference configuration (Spruce density 405kg m^{-3} at 12% MC, elasticity tensor of spruce and web/special type particle board 100%, respectively, friction at the top load plates 0.1 and support load plates 0.1). Material parameters given in Section 2.3 refer to the final selected values from this study.

Parameter		Bending test	Shear test	Bearing test
Flange/Spruce elasticity tensor	−20%	−11.3%	−7.3%	−5.1%
	−40%	−23.1%	−15.7%	−11.0%
Flange/Spruce density 405 kg m^{-3}	+55 kg m^{-3}	+8.3%	+7.4%	+6.7%
	−55 kg m^{-3}	−8.6%	−8.3%	−7.8%
Web/Particle board elasticity tensor	−20%	−3.7%	−9.8%	−11.0%
	−40%	−8.1%	−22.0%	−23.9%
Friction at top load plates	0.2	+3.8%	+1.1%	+4.7%
	0.3	+7.9%	+2.3%	+9.8%
Friction at support load plates	0.2	+1.8,%	+2.0%	+1.2%
	0.3	+3.7%	+4.0%	+2.2%

This was investigated in [23], where two wooden samples glued together had a twice as high resistance during the dry cup test and a 3.6 times higher resistance in case of the wet cup test compared to a continuous sample. However, the exact conditions of the adhesive layer including diffusivity, thickness as well as homogeneity (air bubbles, cracks) are not known. In order to estimate the influence of the adhesive joint, the effect must be between the extreme cases, which either completely prevent moisture transport, i.e. neither water vapor nor bound water transport takes place, or offer no resistance, i.e. water vapor and bound water transport are possible to the full extent. The latter case was used in the case of MUF in [17]. However, the 1C-PUR used has some influence on the moisture resistance, as shown in [23]. To account for the effect of the adhesive to some extent, it is assumed that water vapor transport is possible, while bound water transport is prevented by the adhesive. Since the stiffness and strength values of the particle board are also not known and are adjusted to experimental values, the resulting uncertainties from the moisture contents in the small area next to the glue joint do not have a significant influence on the overall results.

2.2.3. Initial conditions

The initial conditions are a temperature T_{ini} of 293.15 K and an initial water vapor concentration $c_{v,ini}$ of 11.2 g m^{-3}, which is determined from the initial relative humidity φ_{ini} of 65%. Based on the initial water vapor concentration the initial bound water concentration $c_{b,ini}$ can be defined from the adsorption isotherm with 47.5 kg m^{-3}.

2.2.4. Boundary conditions

Exchange with the surrounding climate occurs only in terms of water vapor and energy, which can be described with Neumann boundary conditions. In terms of the water vapor concentration, the flux ϕ_v across the boundary is described as

$$\begin{aligned} \phi_v &= k_{c_v}\,(c_v - c_{v,0})\,f_{lum}, \\ k_{c_v} &= \frac{1}{\frac{1}{k_{c_v,surf}} + \frac{1}{k_{c_v,coat}}} \\ k_{c_v,coat} &= D_{air}/s_d \end{aligned} \tag{4}$$

with the film boundary coefficient $k_{c_v,surf}$, which is set to 1 m s^{-1} and the water vapor concentration of the surrounding climate $c_{v,0}$, which is based on a relative humidity of 100%. This is in agreement with [24], where rain-exposed samples were also modeled with a relative humidity of 100% and a "high" value (compared to the value of 1.4E-7 m s^{-1}, which was used when no rain was present) for the film boundary coefficient. The coating is considered according to [7] with Eq. (4). D_{air} denotes the diffusivity of air, as defined in Table A.1 with a value for ξ of 1 and s_d is the water vapor diffusion-equivalent air layer thickness, according to [22]. The front and back ends of the beams, i.e. the end grain surfaces, are sealed.

In addition to the mass transfer, also the energy flux ϕ_T across the exchange surface has to be considered with contributions from thermal and mass transfer effects due to enthalpy changes and is described by

$$\phi_T = k_T\,(T - T_0) + k_{c_v}\,(c_v - c_{v,0})\,f_{lum}\,h_v, \tag{5}$$

with the heat transfer coefficient k_T of 25 W m^{-2} K^{-1} and the temperature of distant air T_0 of 293.15 K.

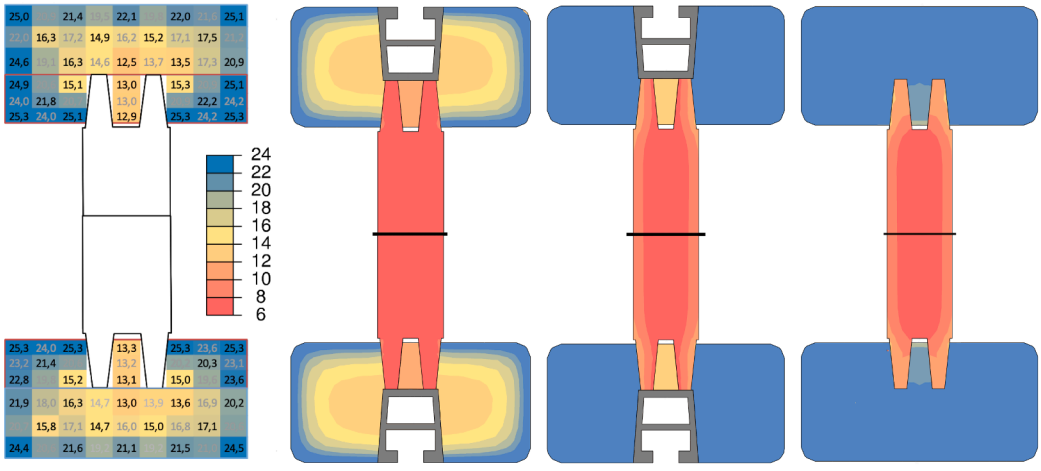

(a) H20 top N - 3d Experimental [38] (b) I tec pro - 3d - moist (c) I tec pro - 60d - wet (d) H20 top P - 60d - wet

Fig. 7. (a) Experimental and (b-d) computed moisture content fields after 3 d and 60 d of exposure of the cross sections to 100% relative humidity at 20 °C. The discontinuity between MCs of the spruce in the flange and the web is a result of the different dry densities. The web is sealed, which leads to smaller changes of the MC, compared to the flange region.

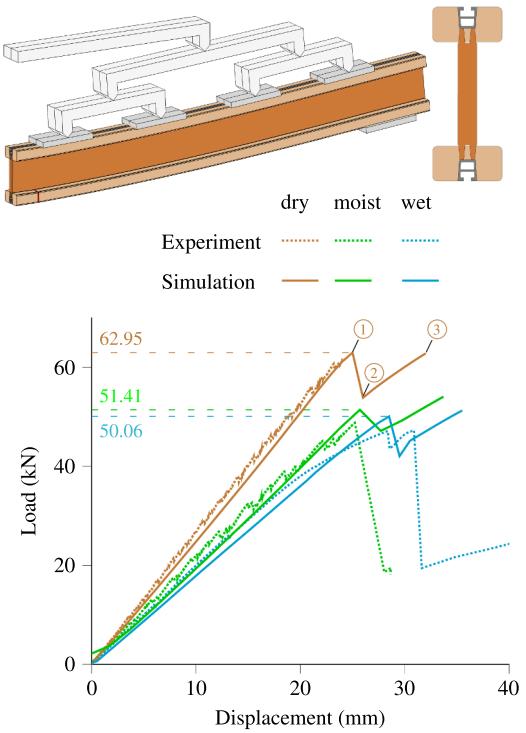

Fig. 8. Load–displacement curves for dry, moist and wet bending resistance tests of the *I tec pro* beam. Experimental curves describe representative samples leading to a median load-carrying capacity. Failure is initiated by a crack due to exceeding the longitudinal tensile strength of the lower flange when the maximum load is reached. Detailed description of the marked states of the different materials is shown in Fig. 9. The top left image shows the dry simulation at ③ with a deformation scale factor of 2.

2.3. Resistance tests

In the following section, the material parameters for the resistance tests are described. In order to correctly model the behavior of the moist and wet beams, not only dry material parameters are presented, but also the moisture dependence has to be considered. Additionally, the interactions between the parts of the cross section are also described as well as the test setups. In the case of the formwork beams presented here, long-term effects are not taken into account because, on the one hand, the maximum load occurs during a short period of time and, on the other hand, the beams are often used at different construction sites and, due to their symmetry, the beams can also be used upside down, which would cause creep in the opposite direction.

2.3.1. Solid timber (spruce)

As described in [17], the material parameters for the elasticity tensor for the wooden flange made of spruce are determined with the continuum micromechanics model of [25,26], where the necessary input parameters are a clear wood density of 405 kg m^{-3} (mean value of samples) and the chemical composition of spruce as well as the moisture content. The model is pre-evaluated for MC levels from 3% to 30% at 1% increments and with the information on the moisture distribution from the previous simulation it is now possible to consider moisture-dependent stiffness properties in each integration point individually. The exemplary elasticity tensor components at 12% MC and 293.15 K are given in Table 1. A cylindrical-orthotropic coordinate system is considered, which is defined with the pith locations in the lower and upper flange, respectively, as shown in Fig. 1.

For moist and wet beams, the coefficients of moisture expansion are defined according to [27] with 0.015%/% in longitudinal, 0.19%/% in radial and 0.36%/% in tangential direction.

A multisurface failure criterion, as subsequently described, was used to model the failure of spruce. In the case of brittle failure, the failure criterion initiates cracking, which is taken into account using the extended finite element method (XFEM), while plasticity is applied in the case of ductile failure.

2.3.1.1. Multisurface failure criterion. Since wood is naturally grown, the resulting irregular structure makes it challenging to describe its failure behavior. An approach to describe the failure behavior at the level of both single cells and the level of annual rings has been studied on a unit cell in [12,14]. Various load combinations were numerically tested and, the main failure characteristics could be characterized. Based on these, a multisurface failure criterion was developed, which is able to describe ductile (plastic) and brittle (cracking) failure mechanisms. The failure criterion is described in terms of multiple Tsai-Wu failure surfaces [28] at the clear wood level as follows:

$$f_i^{cw}(\boldsymbol{\sigma}) = a_{LL,i}\cdot\sigma_{LL} + a_{RR,i}\cdot\sigma_{RR} + a_{TT,i}\cdot\sigma_{TT} + b_{LLLL,i}\cdot\sigma_{LL}^2 + b_{RRRR,i}\cdot\sigma_{RRRR}^2 + b_{TTTT,i}\cdot\sigma_{TT}^2 + 2\,b_{RRTT,i}\cdot\sigma_{RR}\cdot\sigma_{TT} + 4\,b_{RTRT,i}\cdot\tau_{RT}^2 + 4\,b_{TLTL,i}\cdot\tau_{TL}^2 \leqslant 1 \tag{6}$$

The Tsai-Wu tensor components $a_{LL,i}, a_{RR,i}, a_{TT,i}, b_{LLLL,i}, b_{RRRR,i}, b_{TTTT,i}, b_{RRTT,i}, b_{RTRT,i}$ and $b_{TLTL,i}$ are defined according to [14] for all eight failure surfaces, which are depicted in Fig. 2. In case of brittle failure, the multisurface failure criterion controls when and how a crack is initiated. There the direction of the crack normal vector is defined according to the violated failure surface, which for example in the bending load case leads to a crack perpendicular to the grain direction. More details on the implemented approach can be found in [12,14,29].

It can be seen from Fig. 2 that the strength in longitudinal direction is much higher than in transversal direction, with the perpendicular-to-grain tensile strengths being approximately 5 MPa in radial direction and 2 MPa in the tangential one.

To consider the reduction in strength with increasing MC, the following assumptions are made for the moist and wet state:

- For ductile failure, the direction perpendicular to the grain is of primary interest, since the cross sections are compressed in the area of the support load plates. As can be seen from Fig. 7, after 3 days the MC is close to the initial value in large areas of the cross-section, but after 60 days the entire cross section is at 26% MC and thus the strength is reduced by 50% according to [30].
- For brittle failure in case of the bending resistance tests, the maximum tensile strength values of clear wood in longitudinal direction, as shown in Fig. 2, are reduced, on the one hand, to account for irregularities such as possible fiber deviations, knots as well as finger joints (see [31,32]), on the other hand, to account for the current moisture content. The crack is initiated at the outermost fiber, which also exhibits the highest moisture content, as can be seen in Fig. 7. Since the further cracking behavior is brittle, the same strength is applied to the entire cross section. The value is calibrated for each moisture level to predict the experimental load-carrying capacities, resulting in a maximum tensile strength for spruce of 35 MPa in the case of the dry beams, 25 MPa for the moist beams, and 20 MPa in the case of the wet beams. This is again consistent with the bending strength reduction in case of moisture increase as shown in [30].

2.3.2. Particle board

The webs of the cross sections are made of a special type particle board with higher resin content and density compared to other commercial boards of type P7 (heavy duty load-bearing boards for use in humid conditions) according to EN 312 [33]. Failure of the special type particle board is considered quasi-brittle, defined on the basis of a von Mises yield criterion with subsequent softening.

The stiffness parameters in the dry state were measured with

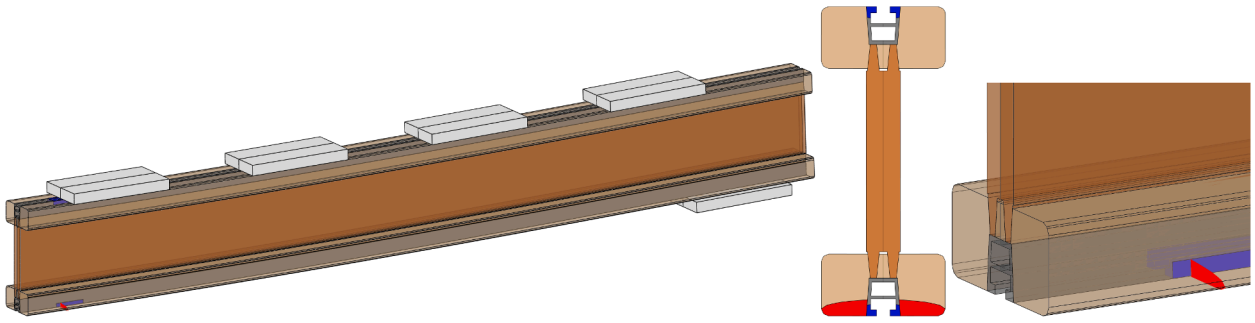

(a) Deformations, plastic zones and crack growth at ① (25 mm displacement)

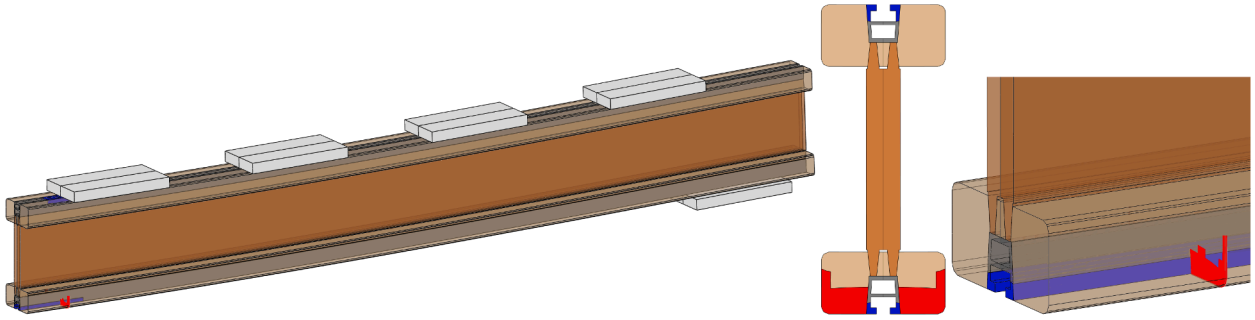

(b) Deformations, plastic zones and crack growth at ② (26 mm displacement)

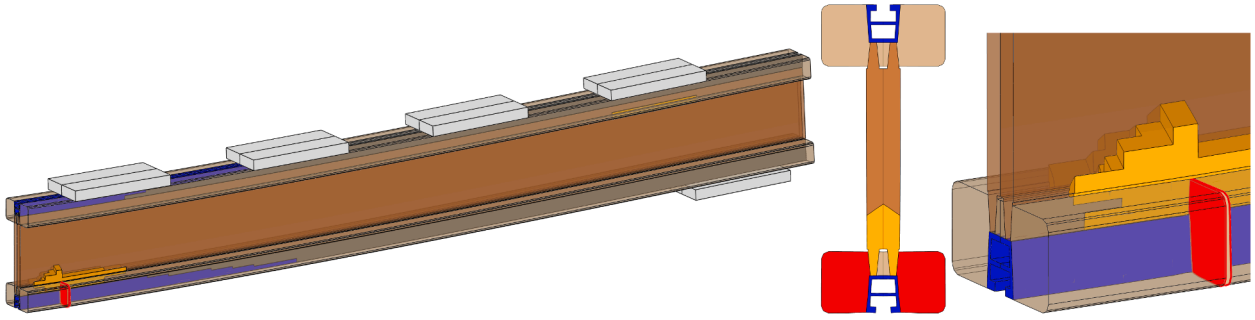

(c) Deformations, plastic zones and crack growth at ③ (32 mm displacement)

Fig. 9. States of plastic zones in the aluminum profile (blue) and particle board web (orange) as well as crack growth (red) in the flange made of spruce at three different displacements of the load transmission construction (shown in Fig. 8) for the bending resistance test of the dry *I tec pro* beam. In each row, the entire model is depicted on the left hand side, followed by a cross section cut at the the crack in the middle and a detail of crack region on the right hand side.

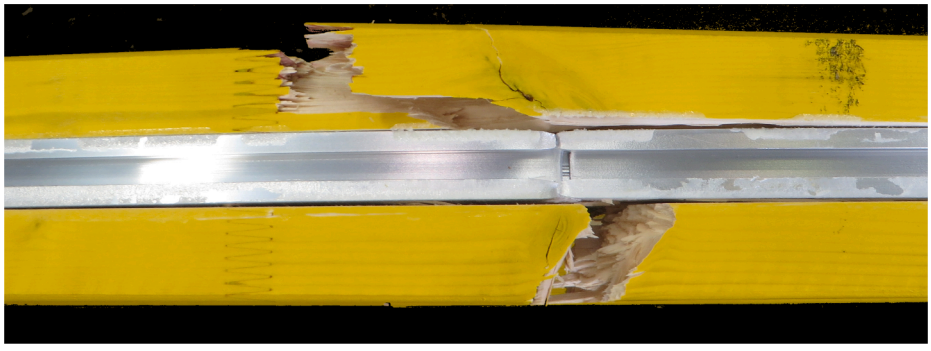

Fig. 10. Failure of the dry *I tec pro* beam in case of the bending resistance test. Both, the aluminum profile and the spruce in the flange show a crack. In the spruce, this crack is related to a knot and the finger joint.

ultrasonic tests according to [34] and calibrated to the experimental load–displacement curves with the sensitivity analysis described in Section 3.1 leading to the values given in Table 2. For the moist and wet simulations, the elasticity tensor was also calibrated, but in contrast to the previous state, all other components were either not moisture-dependent (aluminum profile, load transmission construction) or already determined (spruce). As the goal was to predict the test results in all test setups with the same stiffness reduction factors, the values in

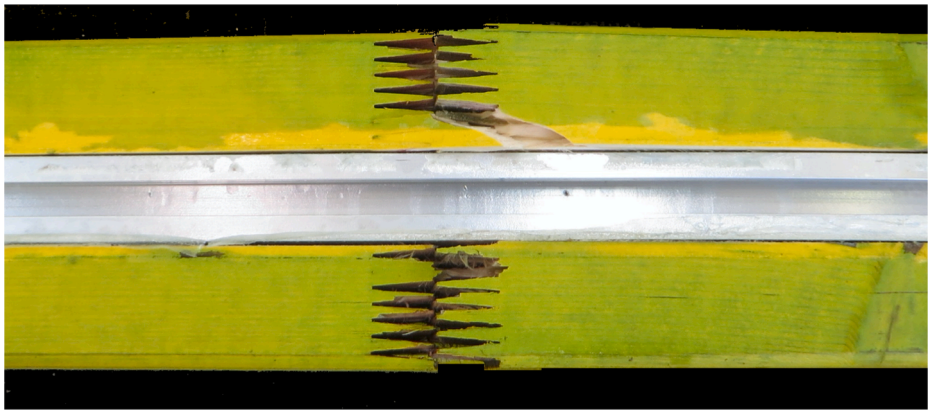

Fig. 11. Failure in the finger joint of the wet *I tec pro* beam in case of the bending resistance test. The aluminum profile did not show a crack in this experiment. In the simulation, the reduced tensile strength accounts for the failure in the finger joint.

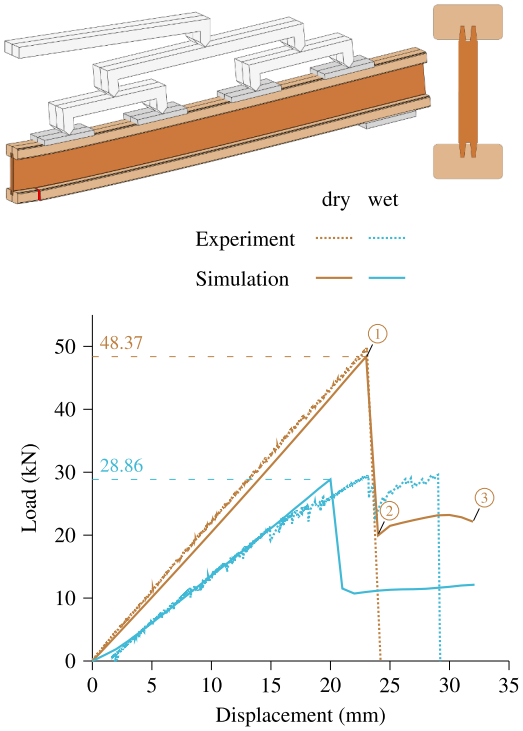

Fig. 12. Load–displacement curves for dry and wet bending resistance tests of the *H20 top P* beam. Experimental curves describe representative samples leading to a median load-carrying capacity. Failure is initiated by a crack due to exceeding the longitudinal tensile strength of the lower flange when the maximum load is reached. Detailed description of the states of the different materials is shown in Fig. 13. The top left image shows the dry simulation at point ③ with a deformation scale factor of 2.

Table 2 were chosen. As can be seen, the values do not differ between the moist and wet state, which is a consequence of the bending tests, where the moist and wet beam show only little differences and also the center part of the web has the same MC due to the sealing, as can be seen from Fig. 7.

However, MC values in the critical joint between the flange and the web change from the moist to the wet state and thus, the values for the yield criterion are adjusted from 32.5 MPa for the dry, to 23.7 MPa for the moist and 14.6 MPa for the wet state. These values were fitted based on the test for shear resistance for the *I tec pro* and then used in all other simulations. From [35] it can be concluded that the strength can be reduced to about 50% of the dry value in case of the bending strength, thus the chosen values seem to be reasonable. A von Mises yield stress of 32.5 MPa corresponds to a shear stress (in case of pure shear) of 18.76 MPa. This value is similar to a fiber board with a density of 800 kg m^{-3} which has a characteristic shear strength in the out-of-plane direction of 16 MPa according to EN 12369–1 [36]. After the yield stress reaches the von Mises yield criterion a subsequent softening takes place and the stresses are reduced to 1 MPa in each moisture state up to a plastic strain of 0.4 and thus, the failure mechanism can be described as quasi-brittle.

The moisture-related expansion coefficients are chosen also according to [37] with 0.035%/% MC for the in-plane and 0.93%/% MC for the out-of-plane direction.

2.3.3. Aluminum

For the profile in the *I tec pro* flange, aluminum of type AW 6060 T66 was used. A tensile experiment with an aluminum sample led to the stress–strain relationship of the whole sample depicted in Fig. 3. This test was also used to calibrate the material parameters to represent this stress–strain relationship by means of finite elements for the resistance tests. Thus, simulations with an element size of 2 mm (as in the resistance tests) were performed to define the ductile material behavior at each integration point based on a von Mises yield criterion with subsequent softening after a yield plateau simulated with the Abaqus model for metal plasticity. The resulting behavior is shown in Table 3. The modulus of elasticity was determined experimentally with 64 GPa and the yield strength with about 220 MPa.

2.3.4. Interactions between components

One goal of this paper is to use the same set of material definitions throughout the series of tests for each moisture state. This also applies to the connection between the flange and the web. During all of the dry and wet state resistance tests, the flanges, the web and the aluminum profiles are connected by tie interactions. The same applies to the wet bending resistance tests. However, in the remaining wet tests for shear and bearing resistance, the stiffness decrease could not be predicted solely by reduced stiffness parameters due to the wetting process. Therefore, additional effects must be considered. Swelling due to wetting of the spruce sections adds additional stresses to the joint, which already exhibits a high amount of shear stress in these two resistance tests. This leads to delamination during load application, as shown in Fig. 16, which reduces the stiffness of the overall beam in addition to the moisture-dependent material parameters. During the experiments, the progress and final state of delamination cannot be fully investigated, since only those visible on the surface can be detected. To account for delamination in the simulations, parameter studies were performed that included partially or fully untied joints and different coefficients of friction in the untied regions of the joints. The configuration determined by the parameter studies must be suitable for both types of beams during

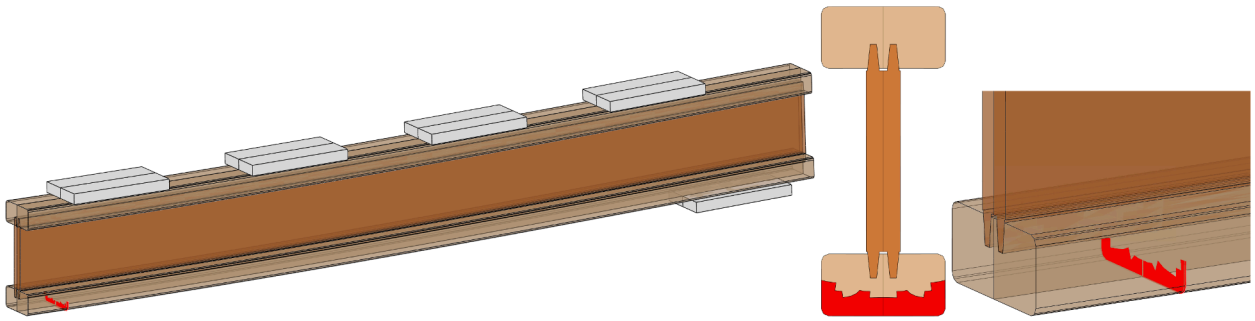

(a) Deformations, plastic zones and crack growth at ① (21 mm displacement)

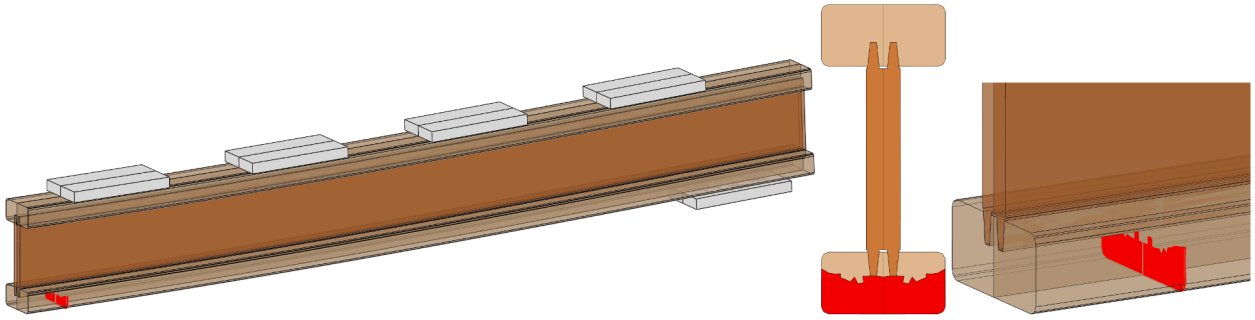

(b) Deformations, plastic zones and crack growth at ② (23 mm displacement)

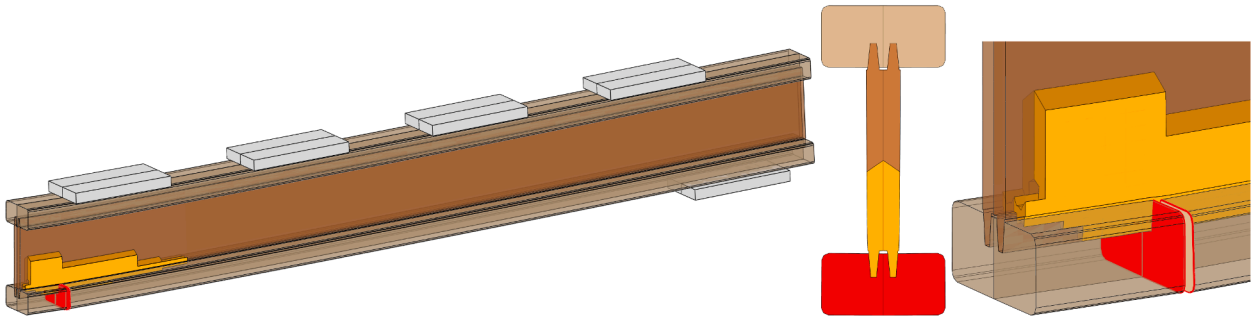

(c) Deformations, plastic zones and crack growth at ③ (32 mm displacement)

Fig. 13. States of plastic zones in the particle board (orange) as well as crack growth (red) in the flange made of spruce at three different displacements (shown in Fig. 12) for the bending resistance test of the dry *H20 top P* beam. In each row, the entire model is depicted on the left hand side, followed by a cross section cut at the crack location in the middle and a detail of the crack region on the right hand side.

the two resistance tests:

- For the *I tec pro*, the tied condition was changed to contact in normal and frictionless in tangential direction in case of the interaction between the flange and the aluminum profile. In the joint between the aluminum profile and the web, also contact in normal direction but a friction coefficient of 0.5 in tangential direction was applied.
- For the *H20 top P* a relative displacement of flange and web was observed during the experiments. Thus, a contact interaction with contact in normal direction and a friction coefficient also 0.5 was applied in the joint between the flange and the web.

As the load-carrying capacity for the bearing resistance test is much higher than for the shear resistance test (three times for the *I tec pro* and two times for the *H20 top P*), the parameter studies led to slightly different results. In case of the test for bearing resistance, this was applied to the entire beam, while for the shear resistance test, these conditions were applied to the section of the beam between the load and the support load plate, where the shear forces are at their maximum. With these adjustments according to the parameter studies, the stiffness decrease in addition to the moisture dependent material parameters could be well reproduced and thus a correct estimation of the beam stiffness could be achieved.

2.3.5. Load transmission construction

With the load transmission construction the forces are applied displacement-controlled onto the investigated beam as prescribed in EN 13377 and shown in Fig. 4–6. In the experiment it consisted of metal beams with hinges on both ends. One construction was used for the test for bearing and bending resistance and another for the test for shear resistance. The beams of the constructions were modeled with a rectangular cross section of 10 × 4 cm and the modulus of elasticity was back-calculated such that the beam's deflection corresponds to the experimental one, which leads to an MOE of 85,585,800 MPa and a Poisson's ratio of 0.3. This MOE does not represent a real material property but is rather a structural property taking into account all stiffness-related effects of the whole construction. The mesh consists of one brick-type element with linear shape functions per cross section to reduce the number of DOF and a length of 4 cm in longitudinal direction.

The plates for the load distribution on the top of the beam and also at the supports are modeled each with 20 cm long, 2 cm thick and 10 cm wide plates, made of steel with a modulus of elasticity of 210,000 MPa

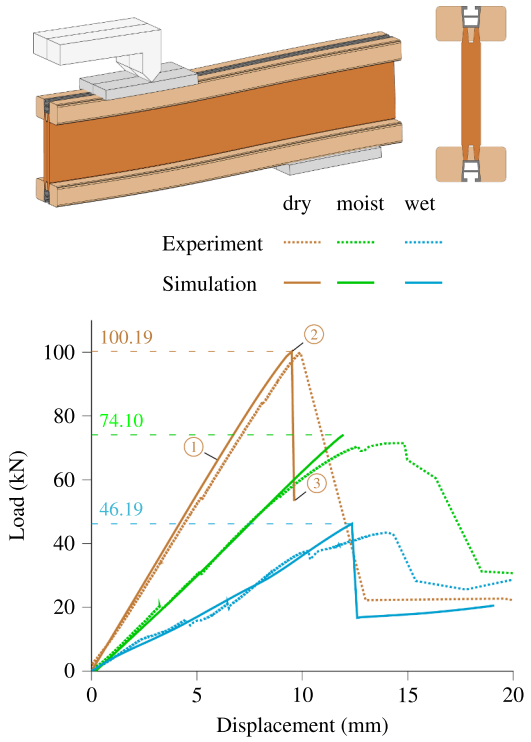

Fig. 14. Load–displacement curves for dry, moist and wet shear resistance tests of the *I tec pro* beam. Experimental curves describe representative samples leading to a median load-carrying capacity. Failure is quasi-brittle and occurring the web next to the joint between the web and the lower flange, when the maximum load-carrying capacity is reached. Detailed description of the states of the different materials is shown in Fig. 17. The top left image shows the dry simulation at ③ with a deformation scale factor of 2.

and a Poisson's ratio of 0.3. According to EN 13377, the top plates for load distribution consist of wooden blocks with at least 4 cm thickness. However, during the computations also steel plates, as previously described, were used, but with an adjusted friction coefficient of 0.15 between the plate and the beam (wood – wood) instead of the 0.10 between the beam and the support load plates (wood – steel). For the mesh of the plates, brick-type elements with a length of 1 cm per direction and linear shape functions were chosen.

2.3.6. Test setup for the bending resistance of EN 13377

According to EN 13377, for testing the bending resistance, a 3.3 m long beam was loaded with eight single forces, which are applied via a load transmission construction as shown in Fig. 4. To reduce the degrees of freedom in the finite element model, only a quarter of the beam was computed during the analysis. In case of this test, the maximum bending moment is expected in the middle of the beam, with the largest shear forces in the area of the supports. The used mesh for the whole model uses 13,023 elements of brick type with linear shape functions in case of the *I tec pro* and 10,307 elements in case of the *H20 top P*. The element size in longitudinal direction is reduced in the region of the maximum bending moment from 4.5 cm to 0.6 cm. The dimensions of the elements within the cross section are between 0.2 and 0.7 cm.

2.3.7. Test setup for the shear resistance of EN 13377

For the test for shear resistance, a 1.50 m long beam was investigated with two single loads applied, as shown in Fig. 5. The setup leads to high shear forces in the section of the beam between the support and the load plate and also a bending moment in the middle of the beam. Again, only a quarter model was analyzed to save computational time. The mesh for the whole model uses 9,729 elements of brick type with linear shape functions in case of the *I tec pro* and 13,530 elements in case of the *H20 top P*. The element size in longitudinal direction is about 2.5 cm and reduced next to the support to 1.8 cm and 1 cm in case of the *I tec pro* and *H20 top P*, respectively. The dimensions of the elements within the cross section are between 0.2 and 0.7 cm.

2.3.8. Test setup for the bearing resistance of EN 13377

The test for bearing resistance has nearly the same setup as the

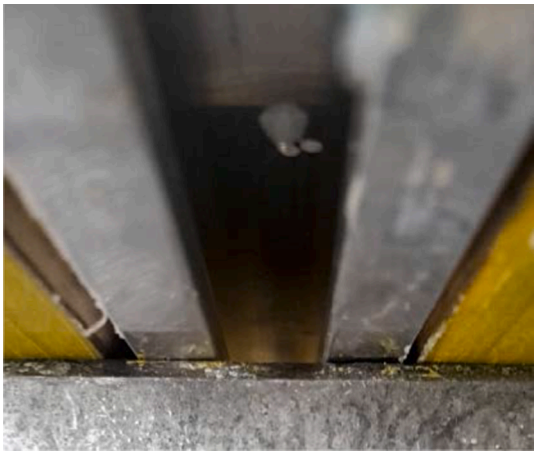

Fig. 16. Delamination of the aluminum profile after loading in case of the wet *I tec pro* beam.

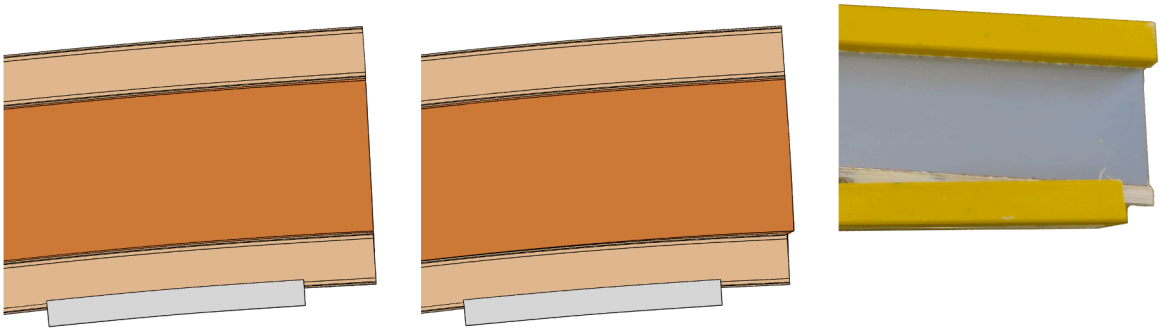

(a) Deformations before failure at ②

(b) Deformations after failure at ③

(c) Experimental failure at the end of the experiment

Fig. 15. Modeled and experimental failure modes in case of the test for shear resistance of the dry *I tec pro* beam with a deformation scale factor of 4 at ② and ③ as shown in Fig. 14. Failure is quasi-brittle and results in a relative displacement of the web and the flange.

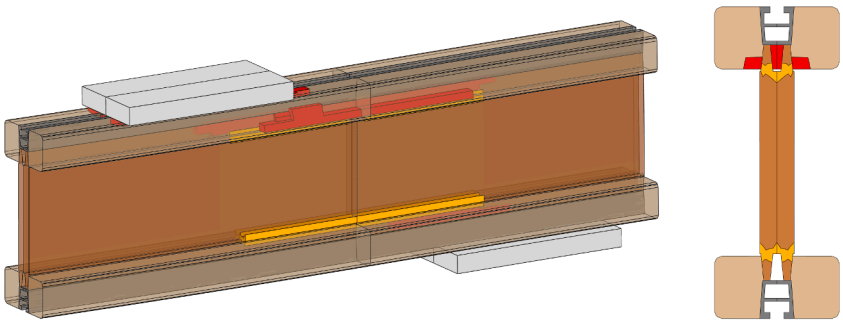

(a) Deformations and plastic zones at ① (6.0 mm displacement)

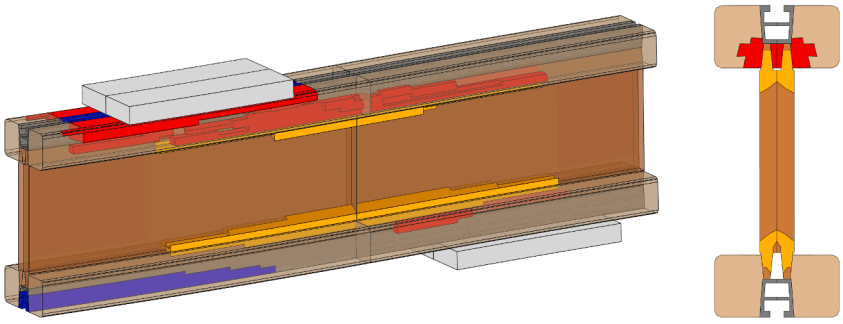

(b) Deformations and plastic zones at ② (9.5 mm displacement)

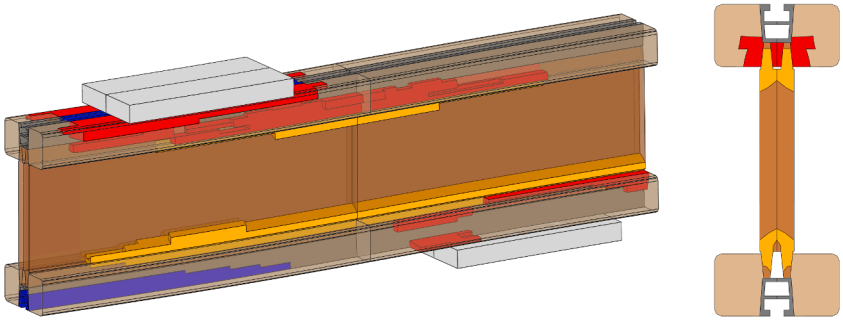

(c) Deformations and plastic zones at ③ (9.61 mm displacement)

Fig. 17. Growth of plastic zones of the aluminum profile (blue), web (orange) and flange (red) at different displacements of the load transmission construction as shown in Fig. 14 during the test for shear resistance of the dry *I tec pro* beam. The cross sections are located in the middle of the model.

previously described bending resistance test, but the supports are placed towards the middle of the beam as depicted in Fig. 6. This leads to large shear forces next to the support and also to negative bending moments in this zone. By utilizing the beam's symmetry, also only a quarter model was computed during the FE Analysis. The mesh for the whole model uses 12,067 elements of brick type with linear shape functions in case of the *I tec pro* and 14,187 elements in case of the *H20 top P*. The element size in longitudinal direction is reduced in the region of the support from 4.5 cm to 2.4 cm in case of the *I tec pro* and to 1 cm in case of the *H20 top P*. The dimensions of the elements within the cross section are between 0.2 and 0.7 cm.

3. Results

In this section the results of the computed resistance tests are presented. A sensitivity analysis is made first to determine the influence of the single parameters on the overall tests and to find a unique set of parameters and material definitions, which predict the results of the different experiments at a certain moisture level. After this, the moisture fields determined with the multi-Fickian transport model are presented followed by a detailed description of the three different tests of the two investigated beams at various moisture levels. The presented experimental load–displacement curves of the different resistance tests and moisture levels lead to load-carrying capacities close to the medians of all available experimental results and are therefore selected to be representative for the characteristic failure mechanism. The *I tec pro* and *H20 top P* were investigated under dry and wet conditions, the *I tec pro* additionally also in the moist state. All the resistance tests were displacement-controlled.

3.1. Sensitivity analysis

To determine a unique set of material parameters and definitions for the entire set of experiments (for each of the three investigated moisture states), a sensitivity analysis was performed.

As Table 4 shows, the various parameters influence the tests in certain directions relative to a reference configuration. A change of the stiffness tensor of the flange material by scaling the tensor by −20% leads to a load-carrying capacity decrease of −11.3% at the same displacement in case of the bending resistance test. Another way to

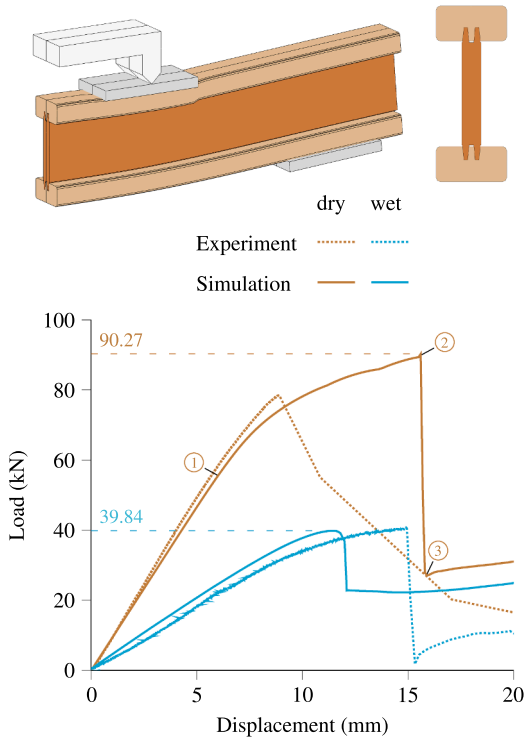

Fig. 18. Load–displacement curves for dry and wet shear resistance tests of the *H20 top P* beam. Experimental curves describe representative samples leading to a median load-carrying capacity. Failure is quasi-brittle and occurring the web next to the joint between the web and the lower flange, when the maximum load-carrying capacity is reached. Details of the states of the different materials are shown in Fig. 19. The top left image shows the dry simulation at ③ with a deformation scale factor of 2.

investigate the influence of the spruce material is to change the density, which leads also to different stiffness properties according to the continuum micromechanics model of [25,26]. The change from the initial density of 405 kg m^{-3} to 460 kg m^{-3} and 350 kg m^{-3} (range according to measurements), respectively, leads to an average stiffness change of + 8.3% respectively −8.6% in case of the test for bending, +7.4% respectively −8.3% for shear and 6.7% respectively −7.8% for bearing resistance. These results are in agreement with the previous method, since the influence on the bearing test was the smallest and on the bending test the largest. In addition to the flange stiffness, also the friction of the top and support load plates have a large influence on the overall system stiffness. In case of the test for bearing resistance, the stiffness of the web and also the friction between the beam and the top load plates influence the system stiffness significantly. In the test for shear resistance, the stiffness of both flange and web have a large influence, whereas the top load plates have only a small influence on the system stiffness. Based on these studies, one set of material parameters and definitions for all investigated experiments of each moisture level was chosen. The stiffness of spruce is defined as moisture-dependent using the continuum micromechanics model of [25,26] evaluated with the mean density of 405 kg m^{-3}. For the other parameters, a reduced stiffness tensor of the web by −20%, a coefficient of friction of 0.15 between the top load plates and the beam, and a coefficient of friction of 0.1 between the beam and the support load plates led to the best results for the dry beams. The parameters and material definitions described in Section 2.3 refer to the values selected in this study.

3.2. Moisture fields

To determine the stiffness and strength of the moist and wet beams, moisture simulations with the multi-Fickian transport model, described in Section 2.2, were made. In Fig. 7 the results of the different beams at the two investigated points in time after 3 and 60 days of exposing the beam to 100% relative humidity are shown. Experimental results of the *H20 top N* beam after three days of exposure were investigated in [38] and are shown in Fig. 7a. This beams shares the same geometry of the flange as the *H20 top P*, but with a different material and dimension of the web. As can be seen when comparing the results after three days of the *H20 top N* and the *I tec pro*, as shown in Fig. 7a and b, respectively, the model is able to predict the results from the experiment in the flanges quite well. After 60 days of exposure, the moisture fields in the spruce parts of both of the modeled cross sections (*I tec pro* in Fig. 7c and *H20 top P* in Fig. 7d) are close to uniform with less than 2% variation in MC within the fields. In contrast to the spruce in the flange, the particle board in the web is sealed and, thus, the reaction to the moistening process is much slower. In the top and bottom zone of the particle board, where the web is connected with a finger joint to the flange, the moisture content increases due to the contact with the spruce material.

3.3. Test for bending resistance

In this section, the results of the test for bending resistance of the two investigated beam types are described. In addition to the dry case, the *I tec pro* beam was also tested under moist and wet conditions and the *H20 top P* beam under wet conditions. For both beam types, the failure mechanism in case of this test was observed to be related to the tensile strength of the lower flange in longitudinal direction. The calculation time was between 1 h and 4 h.

3.3.1. I tec pro

The load–displacement curve of the *I tec pro* test for bending resistance, as shown in Fig. 8, begins with linear-elastic behavior and ends with brittle failure due to exceeding of longitudinal tensile stresses, with a crack starting at the lower edge of the bottom flange. The computed dry beam fails at a displacement of 25 mm with a maximum load of 62.95 kN which is close to the experiment, failing at 61.61 kN and 24.13 mm, respectively. The computed moist beam reaches 51.41 kN at 25.7 mm, while the experiment fails at 48.78 kN and a displacement of 25.21 mm, showing also a good agreement. Under wet conditions the computation reached 50.06 kN at 28.5 mm, which is again close to the experimental value of 47.2 kN at a displacement of 30.8 mm. The difference in stiffness and strength between the moist and wet beam is small, compared to the dry beam, as can be seen in Fig. 8.

Cracking starts at the marked point ① at the location shown in Fig. 9a and continues until the spruce part of the flange is fully cracked, which is depicted in Fig. 9c for point ③. To predict the measured loads from the experiment, the maximum tensile stress for spruce was reduced from 56 MPa in case of clear wood from the model of [14] to 35 MPa to take into account the structure of wood, which is non-homogeneous due to possible knots, fiber deviations or finger joints of the flange and the web, which have to be located in the critical middle section of the beam, according to EN 13377. As soon as the crack initiates, the aluminum profile also shows plastic zones, as shown in Fig. 9a. With the growth of the crack, also the plastic zones get larger (Fig. 9b) until the flange is fully cracked in Fig. 9c. The material behavior of the aluminum profile does not allow for brittle failure, instead the stresses at larger strains are reduced to small values, as shown in Fig. 3. This is the reason for the remaining stiffness in the computation after failure at a displacement of 25 mm. In the experiments, both, the flange and the aluminum profile, showed cracks as depicted in Fig. 10.

For the moist and wet beams, the same model was used, but with different moisture fields, which reduce the stiffness parameters of the flange and the web accordingly. The experiments and also the computations show a similar stiffness for both the moist and the wet state, as depicted in Fig. 8. In the experiment, the failure is located in the finger joints as shown in Fig. 11. This is considered during the computation with the reduced tensile strength, which was set to 25 MPa for the moist

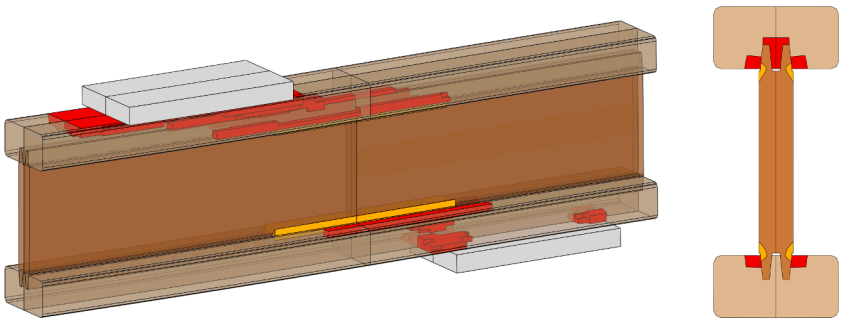

(a) Deformations and plastic zones at ① (6.0 mm displacement)

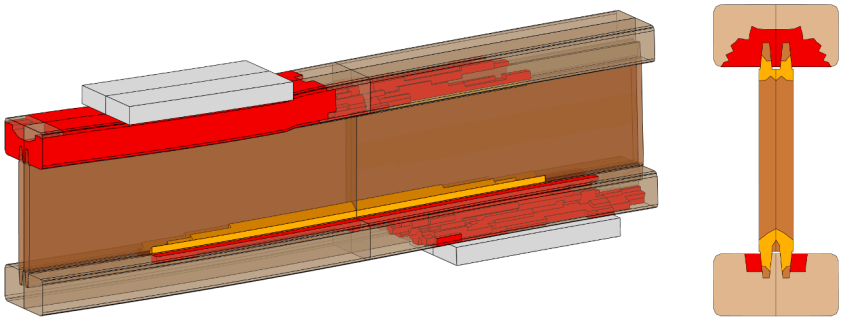

(b) Deformations and plastic zones at ② (15.6 mm displacement)

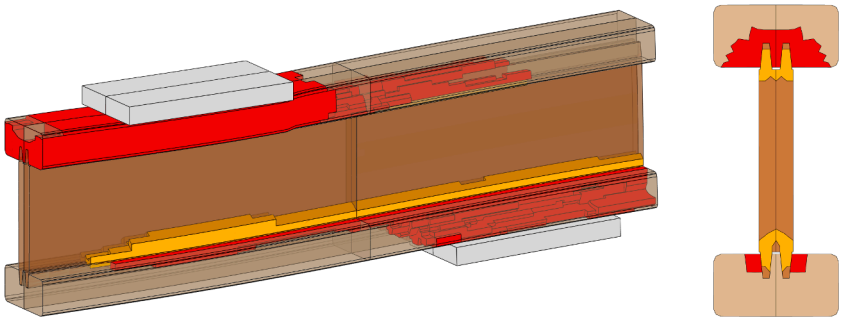

(c) Deformations and plastic zones at ③ (15.7 mm displacement)

Fig. 19. Growth of plastic zones of the web (orange) and flange (red) at different displacements of the load transmission construction as shown in Fig. 18 during the test for shear resistance of the dry *H20 top P* beam. The cross sections are located in the middle of the model.

and to 20 MPa for the wet beam, based on the experimental results. The strength values of the von Mises yield criterion for the special type particle board were also reduced according to Table 2. Again, failure occurs due to exceeding the longitudinal tensile stresses at roughly the same load level for both moisture states, which is caused by the maximum bending stress at the bottom edge of the flange where the values of the moisture contents are quite similar for both cases as can be seen by comparing Fig. 7b and c.

3.3.2. *H20 top P*

The *H20 top P* beam also shows a linear-elastic behavior until brittle failure takes place at a displacement of 21 mm and a maximum load-carrying capacity of 48.37 kN at ① (see Fig. 12) in case of the dry beam computation. This is close to the experimental result, which is 47.76 kN at a displacement of 23.07 mm. Compared to the *I tec pro* beam with the aluminum profile in the flange, the maximum load at time of cracking is lower. As in case of the *I tec pro*, the maximum longitudinal tensile stress was reduced to 35 MPa. The wet beam fails at 20 mm and 28.86 kN as can be seen in Fig. 12 with a maximum longitudinal tensile stress of 20 MPa. This is again in good agreement with the experimental result of 29.4 kN at 23.1 mm.

In case of the dry *H20 top P* beam, the crack is initiated due to longitudinal tensile stresses and is located in the middle section of the beam next to the load plate and begins to emerge from the bottom of the lower flange. At ①, the web shows no plastic behavior as can be seen in Fig. 13a. This is the case until the crack reaches the finger joint in the flange as depicted in Fig. 13b at ②. After that, the web starts to show plastic zones, which increase until the end of the computation at ③, shown in Fig. 13c. This change can also be seen in the load–displacement curve in Fig. 12, where a plateau is reached after the steep drop between ① (21 mm displacement) and ② (23 mm displacement).

For the wet *H20 top P* beam, the same model as in the dry computation was used, but with the reduced stiffness values for the flange and the web based on the moisture field. The failure behavior is similar to the dry beam.

3.4. *Test for shear resistance*

In the following section, the results of the test for shear resistance of the two beams under different moisture conditions are presented. The *I*

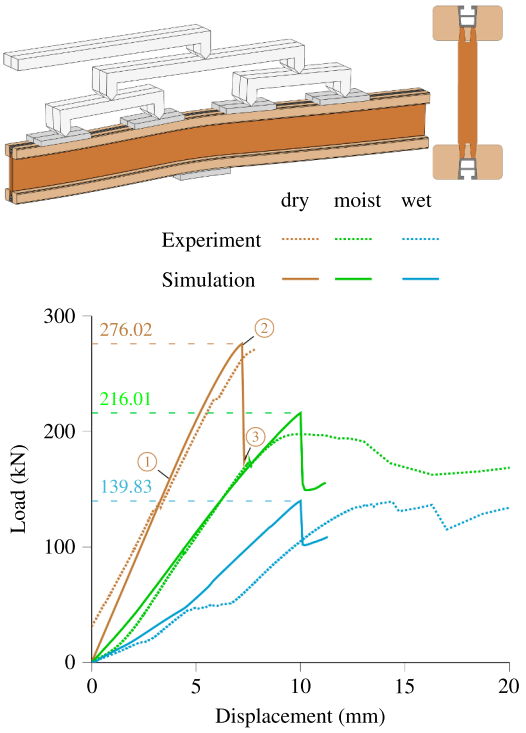

Fig. 20. Load–displacement curves for dry, moist and wet bearing resistance tests of the *I tec pro* beam. Experimental curves describe representative samples leading to a median load-carrying capacity. Failure is quasi-brittle and occurring the web next to the joint between the web and the upper flange, when the maximum load-carrying capacity is reached. Detailed description of the states of the different materials is shown in Fig. 21. The top left image shows the dry simulation at ③ with a deformation scale factor of 2.

tec pro beam is, again, simulated under dry, moist and wet conditions, while the *H20 top P* was investigated under dry and wet conditions. Collapse is characterized by the quasi-brittle failure of the web next to the joint between the lower flange and the web. The calculation time was between 3 h and 40 h.

3.4.1. I tec pro

The test for shear resistance leads to high forces in the joint between the web and the flange. In the experiments, the web material plasticizes next to the joint and a relative displacement of the web and the lower flange leads to failure. The dry and the moist beam share the same geometric model, whereas the wet beam also includes a failed glue line between the aluminum profile and the flange material due to the deformations based on the moisture field, which leads to delamination at very low load levels. This behavior could also be observed during the experiments and is depicted in Fig. 16. The maximum load-carrying capacity is reached in the simulation under dry conditions at 100.19 kN with a yield strength in the particle board of 32.5 MPa, under moist conditions a maximum capacity of 74.10 kN is obtained with a yield strength of 23.7 MPa and under wet conditions, the capacity is 46.19 kN with a yield strength of 14.6 MPa according to Table 2. During the experiment, the maximum load-carrying capacities were 99.75 kN in case of the dry, 71.49 kN for the moist and 43.4 kN in case of the wet beam, as shown in Fig. 14.

Under dry conditions, the plastic zones in the web in the area of the joint is growing until the point of failure at ②, as can be seen in Fig. 17. In Fig. 17a, showing point ① at a displacement of 6 mm, plastic strains in the web and also the upper flange arise in the horizontal section of the beam between the top and support load plates. At ② in Fig. 17b, when the maximum load-carrying capacity is reached at a displacement of 9.5 mm, also the aluminum profile shows plastic zones appearing in the middle of the beam, where tensile stresses due to bending arise. After reaching the maximum load-carrying capacity, the plastic zones are growing along the joint between the web and the flange in the particle board until the end of the beam next to the support is reached at ③ at a displacement of 9.61 mm as shown in Fig. 17c. A relative displacement of the flange and the web caused by quasi-brittle failure of the web, as can be seen in Fig. 15, leads to a drop in the load–displacement curve between ② and ③.

In case of the moist beam, the failure mechanisms are similar to the dry beam. However, the wet beam undergoes some significant changes due to the elevated moisture level, leading to moisture-induced deformations in the spruce cross section in the flange zones. After applying the external loads, the spruce and aluminum profile show delamination and thus, the resistance of the cross section is seriously affected, as shown in Fig. 16. In the model, this delamination effect was considered as described in Section 2.3.4 and able to predict the behavior of the wet beam, as can be seen in Fig. 14. In addition to the delamination, the failure behavior is the same as described for the two other moisture states with quasi-brittle failure of the web leading to a drop in the load–displacement curve, after the maximum load-carrying capacity of 46.19 kN is reached.

3.4.2. H20 top P

The *H20 top P* beam, without the aluminum profile, shows the load–displacement behavior depicted in Fig. 18. The dry beam reaches a maximum load-carrying capacity of 78.41 kN at a displacement of 8.9 mm, whereas the computed beam reaches 90.27 kN at a displacement of 15.6 mm. The experimental and the computational failure are both quasi-brittle due to the particle board and result in a relative displacement between the web and the lower flange. This is shown in Fig. 15 for the dry *I tec pro* beam and this is also the failure mode in case of the wet *H20 top P* beam, but with a highly reduced stiffness due to the increased moisture contents and the interaction between the flange and the web, which is defined with a friction coefficient of 0.5 in the section of the beam between the load and support load plates. The wet beam in the experiment reaches a maximum load-carrying capacity of 40.47 kN at a displacement of 15 mm. The computation is able to predict the maximum load-carrying capacity with 39.8 kN at a displacement of 11.4 mm.

In Fig. 19 the failure behavior of the dry *H20 top P* beam is shown at three characteristic steps. The plastic zones start to emerge at a displacement of 5.2 mm next to the joint of the flange and the web. They increase with ongoing displacement of the load transmission construction as can be seen in Fig. 19a, where the load–displacement curve starts to deviate from the linear-elastic behavior at ①. The maximum load-carrying capacity is reached at a displacement of 15.6 mm at ② with large plastic zones in the flanges next to the support and the load plate as well as in the joint between the web and the flange, as shown in Fig. 19b. As in case of the *I tec pro* beam, the plastic zone in the web next to the joint to the lower flange further grows when the displacement is increased and the beam fails, when the plastic zone reaches the end of the beam next to the support, as shown in Fig. 19c at ③ after the steep drop in the load–displacement curve.

For the wet beam, the stiffness is much lower in comparison to the dry beam. This can not be explained by the reduced stiffness values for the flange and web based on the moisture field alone. The investigation of different definitions of the joint between flange and web has shown that the stiffness could be reached if the joint is modeled with a contact definition with a friction coefficient of 0.5 for the region between the load and the support load plates, as described in Section 2.3.4. The main failure mechanism is, again, the quasi-brittle failure of the web, which leads to a relative displacement of the web and the lower flange.

3.5. Test for bearing resistance

In this section, the results of the test for bearing resistance are

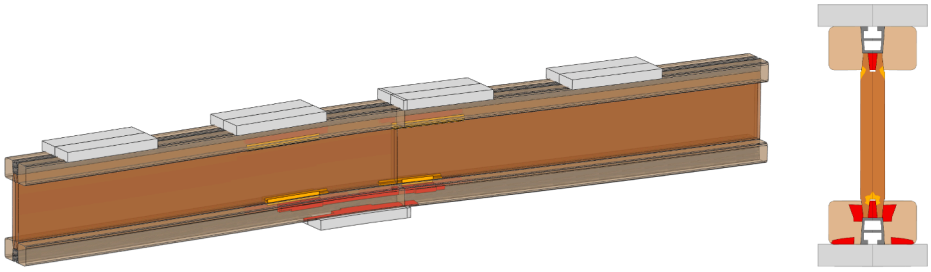

(a) Deformations and plastic zones at ① (3.7 mm displacement)

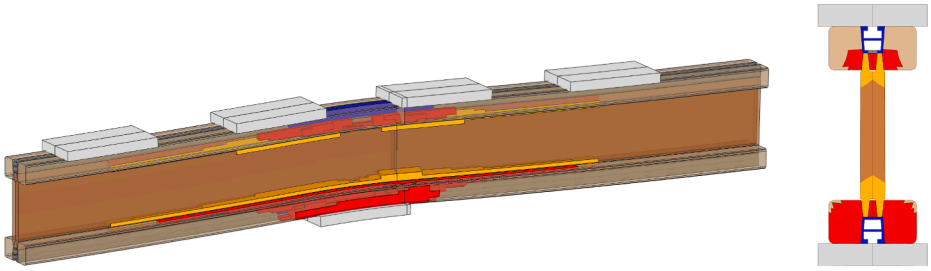

(b) Deformations and plastic zones at ② (7.2 mm displacement)

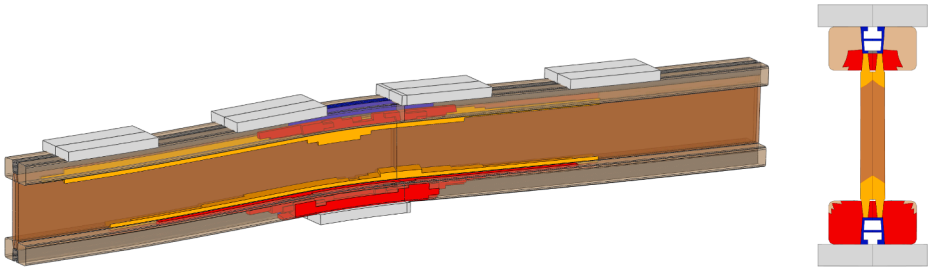

(c) Deformations and plastic zones at ③ (7.3 mm displacement)

Fig. 21. Growth of plastic zones of the aluminum profile (blue), web (orange) and flange (red) at different displacements of the load transmission construction as shown in Fig. 20 during the test for bearing resistance of the dry *I tec pro* beam. The cross sections are located next to the end of the support load plate.

presented. The *I tec pro* beam is investigated under dry, moist and wet conditions and the *H20 top P* is tested under dry and wet conditions, with the moisture fields shown in Fig. 7. Collapse is characterized by the quasi-brittle failure of the web next to the joint between the upper flange and the web. The calculation time was between 1 day and 4 days.

3.5.1. *I tec pro*

The load–displacement curves begin with a linear-elastic region and end with failure at ②, as can be seen in Fig. 20. The dry *I tec pro* reaches the maximum load-carrying capacity of 276 kN at 7.2 mm. In case of the moist beam the maximum load-carrying capacity is 216 kN at a displacement of 10 mm and the wet beam fails at 139.8 kN and also 10 mm. The maximum load-carrying capacities are in good agreement with the experimental values, which are 271.1 kN for the dry, 197.8 kN for the moist and 139 kN for the wet beam. During the wetting process of the wet beam, non-uniform swelling of the spruce parts occur. As a result, the aluminum profile is not in contact with the support load plate at the start of loading. Load application moves the aluminum profile back towards the support load plate until the aluminum profile is back in contact with the support load plate at a displacement of approximately 4.6 mm and after which stiffness increases. At this point, also delamination, as shown in Fig. 16, occurs, which is considered during the simulation with contact in normal direction and frictionless in tangential direction between the aluminum profile and the spruce as well as a friction coefficient of 0.5 instead of the tie condition between the web and the aluminum profile, as described in Section 2.3.4.

In case of the dry beam, after the linear-elastic region, first, the flange starts to plasticize at 2.6 mm. Shortly after that, at 3.5 mm, the web and at 3.7 mm also the aluminum profile show plastic zones, as depicted in Fig. 21a at ① in the region of the support, where the largest vertical loads are to be expected. At the point of failure at ② (7.2 mm displacement), large parts of the spruce and the aluminum profile in both flanges as well as the web show plastic zones next to the support, as can be seen in Fig. 21b. While the plastic zones in the lower flange occur because of vertical loads, in the upper flange also tension due to the negative bending moment can be observed. The forces are transferred from the load plate via the aluminum profile to the web and further via the aluminum profile into the load plate, as can be seen from the depicted plastic zones in the cross sections. At ③ (7.3 mm displacement) the plastic zones in the web next to the finger joint between the upper flange and the web are growing rapidly towards the middle of the beam, which leads to the drop in the load–displacement curve, as can be seen when comparing Fig. 21b at ② with Fig. 21c at ③.

For the moist beam the same model as for the dry one was used, but with a reduced stiffness for the spruce in the flanges and the particle board in the web. The strength for the moist web was reduced from 32.5 MPa in case of the dry beam to 23.7 MPa according to Table 2. The main failure mechanism in the joint between web and flange, is similar as observed for the dry beam.

In case of the wet beam, the moisture field leads to a deformation of the cross section, as previously described, with only the top and bottom edges of the spruce touching the load and support load plates, respectively. After 4.6 mm of displacement, the beam is compressed thus far that the aluminum profile touches the load plates and forces can be

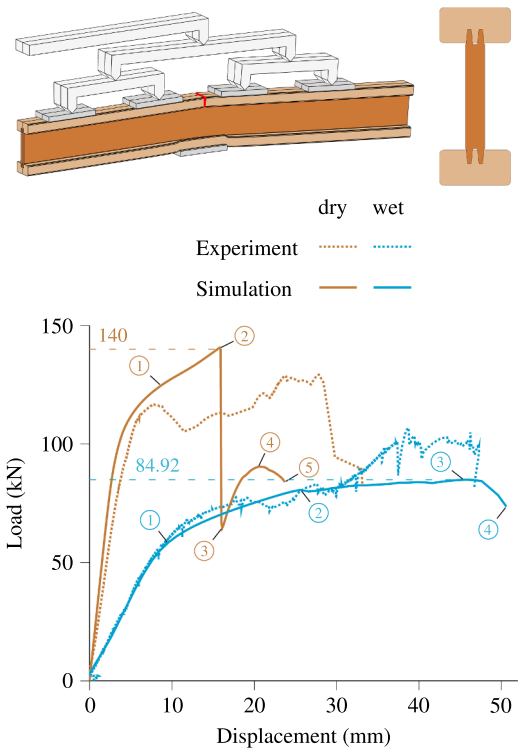

Fig. 22. Load–displacement curves for dry and wet bearing resistance tests of the *H20 top P* beam. Experimental curves describe representative samples leading to a median load-carrying capacity. Failure is quasi-brittle and occurring the web next to the joint between the web and the lower flange, when the maximum load-carrying capacity is reached. Detailed description of the states of the different materials is shown in Fig. 23 and Fig. 24, respectively. The top left image shows the dry simulation at ⑤ with a deformation scale factor of 1.

transferred directly into the support load plate. This point is marked with the mentioned kink in the load–displacement curve in Fig. 20. In addition to the different moisture field, also the interaction between the aluminum profile and the surrounding materials was changed, as described in Section 2.3.4. In the particle board the maximum stress for the failure mechanism was reduced to 14.6 MPa, as in the previous examples. To account for the strength reduction in case of moist wood, the plastic yield stress was reduced by 50% according to Section 2.3.1.1. The resulting failure mechanism is then similar to the dry and moist computation.

3.5.2. *H20 top P*

In case of the *H20 top P* beam, the low stiffness of wood perpendicular to the grain direction reduces the overall stiffness of the beam in comparison to the *I tec pro*, where the load was transferred via the, in comparison stiffer, aluminum profiles. The maximum load-carrying capacity in case of the dry simulation is reached with 140 kN at a displacement of 15.9 mm and in case of the wet beam 84.92 kN at 45.6 mm, as shown in Fig. 22. While the dry beam shows a drop in the load–displacement curve at 25.3 mm, the wet beam exhibits a yield plateau until failure occurs. The experimental results show a plateau beginning after a first peak with a load-carrying capacity of 116.7 kN at a displacement of 7.3 mm and reach the highest values at 129 kN at a displacement of 27.6 mm in the dry case. The wet experiment shows a very good agreement to the computations until 30 mm of displacement and reaches the maximum load-carrying capacity after an increase after 30 mm at 106.8 kN at a displacement of 38.8 mm.

The load–displacement curves of the dry beam show a decrease in stiffness as the spruce in the lower flange starts to plasticize at a displacement of about 1.1 mm until at ① (8.5 mm displacement) nearly the whole cross section of the lower flange shows ductile behavior in the region around the support load plate, as can be seen in Fig. 23a. Also a crack starts to emerge in the upper flange together with plastic zones next to the load plates. At ② (15.9 mm displacement) the maximum load-carrying capacity of 140 kN is reached. The web shows plastic zones only in the joint above the support and the crack has further increased, as can be seen in Fig. 23b. The upper flange is fully cracked at ③ at a displacement of 16.1 mm, leading to a drop in the load–displacement curve. Plastic zones are now also showing up in the web next to the crack, as depicted in Fig. 23c. The load-carrying capacity increases slightly after the drop and reaches 90.43 kN at ④ (20.7 mm displacement) while the plastic zones in the web increase and stay constant in the web, as shown in Fig. 23d. At ⑤ at a displacement of 23.7 mm the plastic zones in the web cover nearly the full height, while those of the flanges stay about the same (see Fig. 23e).

In case of the wet beam the stiffness is smaller due to the reduced stiffness of the spruce in the flange and the web. Also the joint between the flange and the web is modeled with contact and friction properties instead of a tie constraint. After a short sequence of linear-elastic behavior, the web starts to plasticize and also the spruce shows ductile behavior next to the support, as can be seen in Fig. 24a at ① (9.6 mm displacement). Further increase of the displacement of the load transmission construction leads to extending plastic zones in both materials around the support. After ②, at a displacement of 25.6 mm with the plastic zones depicted in Fig. 24b, the load level is only slightly increasing. The web now also shows large plastic zones in the area of the support. This behavior continues until ③, where the maximum load-carrying capacity is reached at a displacement of 45.6 mm with 84.92 kN. The corresponding plastic zones (shown in Fig. 24c) are now enlarged, especially in the web in the area around the support, where almost a plastic hinge is established. Also the lower flange is moving away from the rest of the cross section at the free end of the beam, which is only connected by frictionless contact to the rest of the beam. At ④, the plastic hinge is fully established, as can be seen in Fig. 24d at a displacement of 50.6 mm.

4. Discussion

The moisture field simulations, shown in Fig. 7, gave good results compared to the experimentally determined moisture fields in the spruce part of the flange. No experimental data were available in the web for comparison. Since the multi-Fickian model has not been used previously for the particle board, the transport properties had to be determined using assumptions and comparisons of values from the literature. While water vapor transport was reduced to account for the effects of glue and compaction during the manufacturing process, bound water was not reduced, resulting in higher moisture contents within the board. However, the numerically obtained moisture field of the particle board has no influence on the material parameters regarding stiffness and strength, since no moisture-dependent properties were available and calibrated properties on the basis of the experimental behavior of the resistance tests were used. In contrast, the deformation behavior of the cross section is influenced by the moisture field. The glue of the particleboard is not directly accounted for in the material parameters, resulting in possibly too large bound water diffusivities. This results in higher MCs predicting larger deformations as well as stresses, leading to results on the safe side with respect to the failure mechanisms. As can be seen from Fig. 7, although higher bound water transport properties were used, the changes in the moisture field are small compared to spruce. Thus, overall, the effects of the assumptions made in determining the moisture field in the particle board on the results of the resistance tests are only minor.

All used material parameters and definitions, which were either obtained from literature, back-calculated from experiments or calibrated based on the resistance tests, are summarized below:

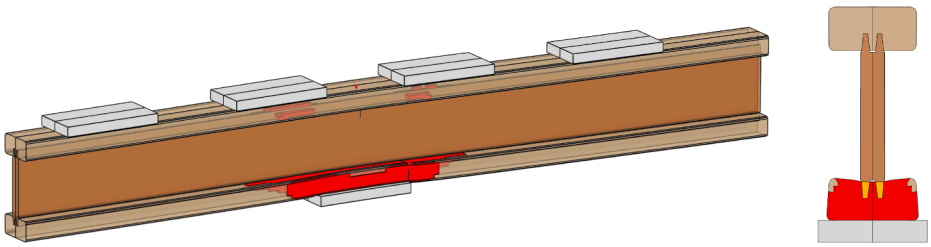

(a) Deformations and plastic zones at ① (8.5 mm displacement)

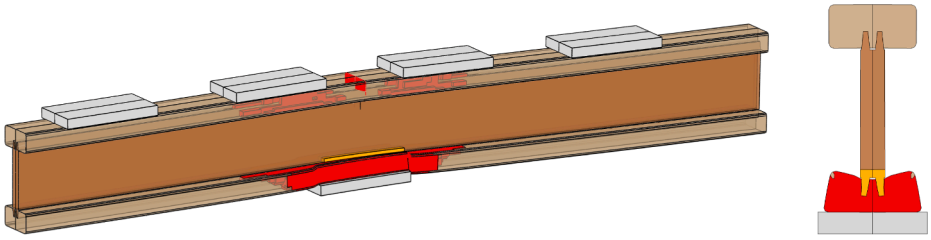

(b) Deformations and plastic zones at ② (15.9 mm displacement)

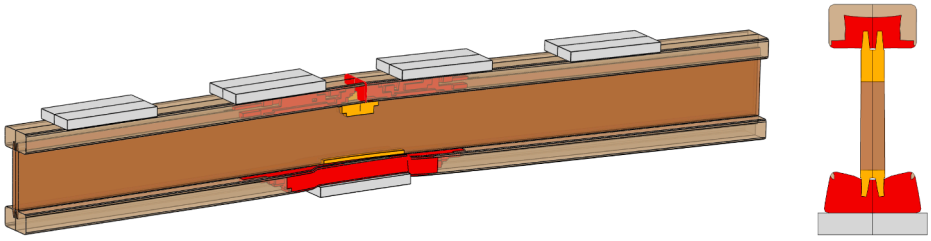

(c) Deformations and plastic zones at ③ (16.1 mm displacement)

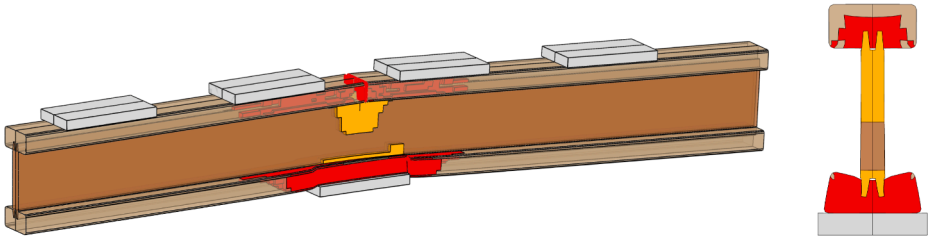

(d) Deformations and plastic zones at ④ (20.7 mm displacement)

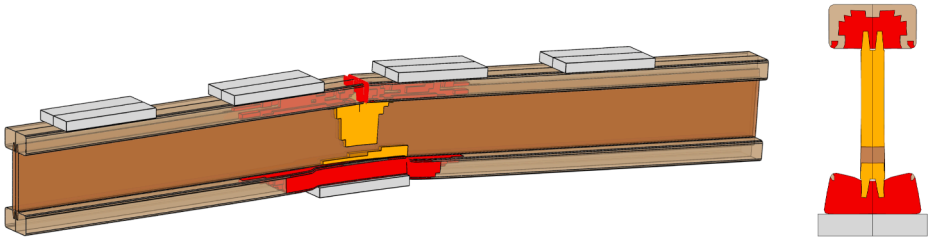

(e) Deformations and plastic zones at ⑤ (23.7 mm displacement)

Fig. 23. Growth of plastic zones of the web (orange) and flange (red) at different displacements of the load transmission construction as shown in Fig. 22 during the test for bearing resistance of the dry *H20 top P* beam. A crack emerges in the upper flange in the region of the support. The cross sections are located in the middle of the support load plate, next to the crack location.

- *Load transmission construction:* The stiffness values were back-calculated according to the deflection behavior determined by a static analysis of the experimental construction.
- *Aluminum profile:* Stiffness and plastic material behavior were back-calculated according to a tensile test on an aluminum sample.
- *Spruce:* Stiffness was defined using the continuum micromechanics model of [25,26]. Strength values in longitudinal direction, crucial for the maximum loading capacity of the bending resistance tests, were calibrated for each moisture state. The resulting strength reduction between the states leads to a close-to-linear relationship that is in agreement with [30].
- *Particle board:* This board is of special type with a higher density and resin content. The stiffness parameters for the dry tests were calibrated on basis of ultrasonic measurements and a sensitivity analysis.

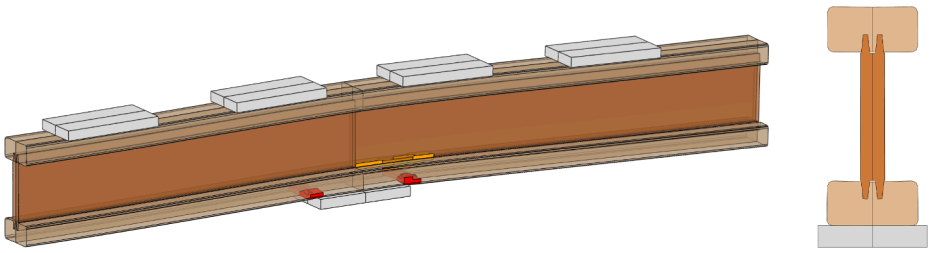

(a) Deformations and plastic zones at ① (9.6 mm displacement)

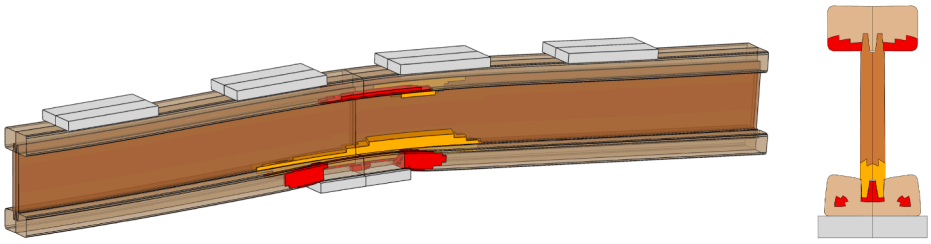

(b) Deformations and plastic zones at ② (25.6 mm displacement)

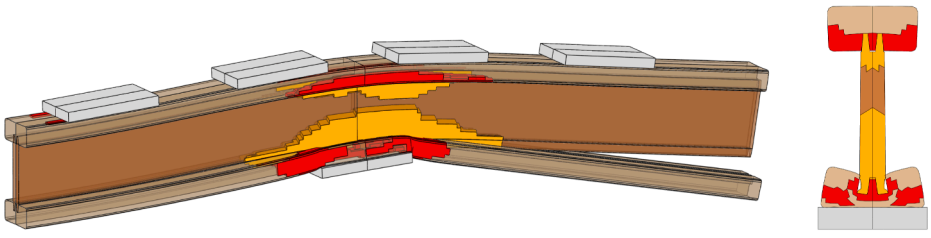

(c) Deformations and plastic zones at ③ (45.6 mm displacement)

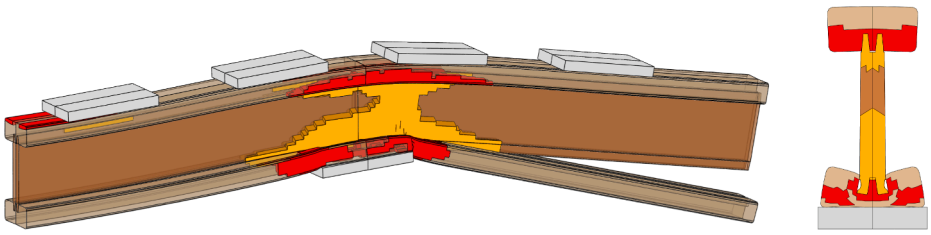

(d) Deformations and plastic zones at ④ (50.6 mm displacement)

Fig. 24. Growth of plastic zones of the web (orange) and flange (red) at different displacements of the load transmission construction as shown in Fig. 22 during the test for bearing resistance of the wet *H20 top P* beam. The cross sections are located in the middle of the support load plate.

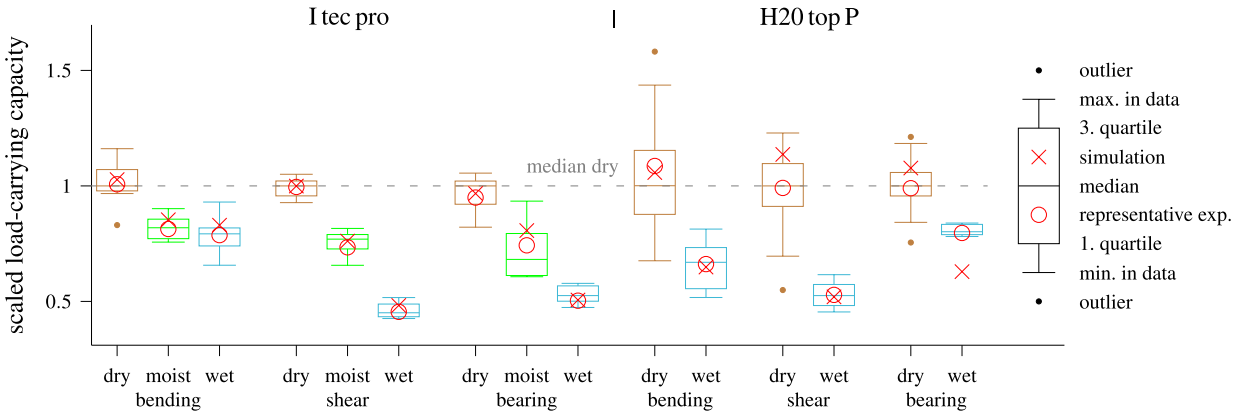

Fig. 25. Comparison of maximum, median and minimum load-carrying capacities from experimental tests with the results from the simulations and chosen representative experiments. In case of the *I tec pro* ten beams for each moisture state were experimentally tested and in case of the *H20 top P* beam 56 samples for the bending and bearing as well as 61 beams for the shear resistance test were analyzed for dry conditions and six beams each for wet conditions. The values are scaled to the median of the respective dry experiments.

In the moist state only the particle board stiffness is the remaining parameter that was calibrated. The moist and wet stiffness of the entire beam in the bending resistance test differ only slightly and therefore the same value was chosen for the wet state. A von Mises yield criterion with subsequent softening is used to model the failure behavior. The yield strength was calibrated based on the shear resistance test of the *I tec pro* for each moisture content and then also used in the test for bearing resistance as well as for the other beam type, predicting also correct load-carrying capacity levels and failure mechanisms.

- *Friction between beams and load plates:* The values were determined based on the sensitivity analysis presented in Section 3.1 for the dry tests such that good results could be predicted for all three resistance test setups as well as both beam types and were also used in the other states subsequently. The value between wood and wood for the top load plates was chosen higher than the support load plates (wood - steel).
- *Joint lines:* Were assumed to be tied in all test setups and beams, except for the wet beams in bearing and shear. Since the stiffness between the moist and the wet state differs significantly for these in contrast to the bending resistance test and cannot be explained solely by the moisture-induced stiffness decrease of the material parameters, the joint lines, which do not influence the bending resistance test due to the lower loading level, were investigated in more detail and optimized, resulting in (partially) delaminated joint lines, which were also observed during the experiments.

In Fig. 25, the experimental and numerical results of all investigated beams are shown using box and whisker plots. As can be seen, the chosen sets of material parameters and definitions as well as geometric conditions are able to predict the experimental results in a very good manner for all the 15 different settings. The selected load-carrying capacities of the representative experimental curves are in good agreement with the median capacity of the beams of the respective experiment. During the experiments, the finger joints in the flange and also the web have to be placed in the critical sections. To account for this, the strength values for spruce during the simulation for bending resistance and for the web were adjusted accordingly. In case of the test for bearing resistance of the wet *H20 top P* beam, the results are slightly off the experimental ranges. However, as can be seen from Fig. 22, the load–displacement curve can be reproduced in a very good way up to 30 mm of displacement. In the last section of the experiment, the beam shows a slight increase in the load-carrying capacity, which could not be reproduced in the simulations and, thus, the shown results depict smaller values than observed during the experiments.

Comparing the *I tec pro* with the *H20 top P* beam during the test for bending resistance, both beams show the same failure characteristics, which are based on exceeding the longitudinal tensile strength of the lower flange. The aluminum profile of the *I tec pro* leads to a larger stiffness in the linear-elastic region. For the *I tec pro* beam, the results under moist and wet conditions differ only slightly, compared to the dry beam, as shown in Fig. 8. This is caused by the moisture fields, which show similar MC values in the zone close to the boundary, where the crack initiates, according to Fig. 7. This is also the reason why the stiffness tensor for the web from Table 2 under moist and wet conditions was chosen to be equal. Experimentally, the moist and wet beams show failure in the finger joints in the area of the flange, according to Fig. 11, which is accounted for with a reduction in tensile strength for spruce. Also, only in case of the dry beam, the aluminum profile showed cracks.

The test for shear resistance was used to calibrate the yield strength of the quasi-brittle failure behavior of the secial type particle board in the web, which was then also used in all other simulations. The chosen strength was able to predict the failure modes of the test for shear and bearing resistance. While the moist model used the same geometry as the dry version, additional adjustments had to be made for the wet beam to match the stiffness of the experimental beam, as the decrease could not be explained by the moisture-induced decrease in material parameters and definitions alone. The wet beam exhibits delamination behavior between the aluminum profile and the web as a result of moisture increase and external load application, as shown in Fig. 16. This was accounted for by modifying the joints as shown in Section 2.3.4. With these adjustments, the stiffness could be well reproduced, as can be seen in Fig. 14. This concept was also used in case of the wet *H20 top P*, leading again to good results, as shown in Fig. 18.

The stiffness in the linear-elastic region of the dry test for bearing resistance of the two investigated beams show a very similar behavior. This changes in case of the *H20 top P* at about 100 kN of loading, as the wooden flange starts to show ductile behavior, as the wood gets compressed due to the perpendicular to the grain loading. This effect is much smaller in case of the *I tec pro* beam, since the forces get transferred from the particle board via the aluminum profile into the support load plate, thus the failure mode of this beam shows less ductile behavior, as can be seen when comparing Fig. 20 with Fig. 22. While the dry model was used for the simulation in the moist state, additional adjustments were made for the wet beams compared to the dry as described in Section 2.3.4. This enabled the models to predict the stiffness and maximum load capacity of the wet beams, as shown in Fig. 20 and 22 respectively. In case of the *I tec pro* beam, the point at about 4.6 mm of displacement, where the aluminum profile gets back in contact with the support load plate and the stiffness increases, could also be reproduced.

5. Conclusion & outlook

When developing a new wood composite beam, various experiments must be performed, which are complex and time consuming. In case of prefabricated timber formwork beams these experiments are defined in EN 13377. In addition to a test under dry conditions, also different moisture states must be considered to evaluate the behavior of the beams. In this work, a numerical concept is proposed, able to support this complex experimental program and to significantly reduce it in the medium term. Moisture fields are determined based on a hygrothermal multi-Fickian transport model, which includes heat and mass transfer within spruce, particle board and also aluminum. The interactions between these materials were also taken into account. In a second step, different resistance tests, as specified in EN 13377, were performed numerically. Different failure mechanisms, in some cases also dependent on the moisture state, could be described appropriately. Especially in case of wet beams, which were exposed for 60 days to a climate of 100% relative humidity, the delamination between the aluminum profile and the wooden flange showing up during the loading process, which is crucial for the beam stiffness under such conditions, could be simulated realistically. In order to address the variations in the experimental test results, the results from the simulations were compared with selected representative tests with median load-carrying capacities. When calibrating the unknown parameters, a set was defined that leads to good agreements for all three experimental results and both investigated beam types at one moisture level. The stiffness tensor of spruce was defined as moisture dependent with its mean density as input parameter for the continuum micromechanical model.

The main findings are emphasized as follows:

- With the adjustments shown, it was possible to use the multi-Fickian transport model for the entire cross section, including the particle board as well as the interaction between the different wood products. The simulated moisture field agreed well with the experimental one in the experimentally investigated part of the cross section.
- The moisture field was also used for the prediction of stiffness decrease of the spruce. The moisture-dependent properties of the special type particle board, which was the remaining unknown in the wet and moist states, were adjusted to reproduce the stiffness decrease accordingly. In the wet state, additional considerations

regarding the delamination of the joint were necessary for the shear and bearing resistance tests.
- Brittle failure modes in the spruce using the extended finite element method (XFEM), ductile failure modes in the spruce, quasi-brittle failure modes in the special type particle board as well as ductile failure modes in the aluminum profile were used to reflect the actual behavior of the beams and to reproduce the load-carrying capacities and failure modes of the different setups.

Long-term effects were not taken into account for these beam types, since the maximum load occurs only during a rather short time after the concrete is poured in the formwork. However, similar beams are also used for other purposes, e.g. for floors or roof structures, where long-term effects could play a role. The assumptions made in the modeling regarding the modeling of moisture transport in the particle board as well as the glue in terms of the multi-Fickian model requires experimental investigations.

By using the proposed methods, concepts and the calibrated parameters, it is possible to numerically complement experimental test programs of complex composite wood beams according to EN 13377 in different moisture states to further improve beam geometries.

Data Availability

The raw/processed data required to reproduce these findings cannot be shared at this time as the data also forms part of an ongoing study.

CRediT authorship contribution statement

Maximilian Autengruber: Writing – original draft, Visualization, Software, Investigation, Methodology. **Markus Lukacevic:** Supervision, Conceptualization, Methodology, Writing - original draft, Writing – review & editing, Software. **Gregor Wenighofer:** Conceptualization, Visualization, Methodology, Data curation, Investigation. **Raimund Mauritz:** Conceptualization, Investigation, Supervision, Funding acquisition, Project administration. **Josef Füssl:** Supervision, Conceptualization, Methodology, Writing – review & editing, Funding acquisition, Project administration.

Declaration of Competing Interest

The authors declare that they have no known competing financial interests or personal relationships that could have appeared to influence the work reported in this paper.

Acknowledgments

The funding from the Doka GmbH and the Austrian Research Promotion Agency (FFG, Project Number 857041) is gratefully acknowledged. The authors acknowledge TU Wien Bibliothek for financial support through its Open Access Funding Programme.

Appendix A. Constitutive equations and material parameters

The reference state for the expressions to determine the thermodynamic properties for specific isobaric heat capacities c_p and enthalpies h is set to 273.15 K and 101 325 Pa.

See Tables A.1 and A.2.

Table A.1
Constitutive equations and material parameters used in the model.

Property	Value/Expression	Ref.
Spruce dry density	$\rho_{d,sp} = 405\ \mathrm{kg\ m^{-3}}$	
Particle board dry density (spruce fibers)	$\rho_{d,pb} = 797\ \mathrm{kg\ m^{-3}}$	
Moisture content	$X = \frac{c_b}{\rho_d}$	
Bound water diffusion tensor	$\boldsymbol{D_b} = \boldsymbol{D_0} \exp\left(\frac{-E_b}{R\,T}\right)$	[39]
Bound water diffusion tensor (Soret effect)	$\boldsymbol{D_{bT}} = \boldsymbol{D_0} \frac{c_b\,E_b}{R\,T^2} \exp\left(\frac{-E_b}{R\,T}\right)$	[39]
Activation energy of bound water	$E_b = 38500 - 29000\,X$	[40]
Universal gas constant	$R = 8.314\ \mathrm{J\ mol^{-1}\ K^{-1}}$	
Water vapor diffusion tensor	$\boldsymbol{D_v} = \boldsymbol{\xi}\left(2.31{\cdot}10^{-5} \frac{p_{atm}}{p_{atm}+p_{v_{air}}} \left(\frac{T}{273}\right)^{1.81}\right)$	[19,41,42]
Water vapor pressure	$p_{v_{air}} = c_v \frac{R\,T}{M_{H_2O}}$	
Molar mass of water	$M_{H_2O} = 18.015\ \mathrm{g\ mol^{-1}}$	
Moist density of wood	$\rho_{moist} = \rho_d \frac{1+X}{1+0.84\,c_b}$	[43]
Volume proportion of the cell lumen	$f_{lum} = 1 - \frac{\rho_{moist}}{\rho_{cwm}}$	
Density of the pure cell wall material	$\rho_{cwm} = 1530\ \mathrm{kg\ m^{-3}}$	[3,40]
Spruce conduction tensor	$\boldsymbol{K} = \boldsymbol{K_0}\,(0.142 + 0.46\,X)$	[44]
Heat capacity of the cell wall material	$c_{p_s} = -0.60453 + 0.006714\,T$	[45]
Enthalpy of water vapor	$h_v = 2060.5 + 1.3798\,T + 0.84808{\cdot}10^{-4}\,T^2$	[46]
Specific enthalpy of bound water	$h_b = 4.185\,(T - 273.15\ \mathrm{K}) - 1146.4\exp(-14.48\,X)$	[46,47]
Average enthalpy of bound water	$\overline{h}_b = -1143.1 + 4.185\,T - \frac{79.172\,\rho_d\,(1-\exp(-14.48\,X))}{c_b}$	[46,48,49]

Table A.2
Diagonal components of the material parameter tensors. For the particle board the components 1 and 2 are the in-plane directions and 3 is the perpendicular-to-the-plane direction.

Parameter	Component			Ref.
	L/1	R/2	T/3	
Spruce D_0	$2.5{\cdot}7{\cdot}10^{-6}$	$7{\cdot}10^{-6}$	$7{\cdot}10^{-6}$	[5]
Spruce ξ	0.98	0.07	0.05	[3]
Spruce K_0	2	1	1	[50]
Particle board D_0	$1.875{\cdot}7{\cdot}10^{-6}$	$1.875{\cdot}7{\cdot}10^{-6}$	$7{\cdot}10^{-6}$	
Particle board ξ	0.3	0.3	0.02	
Particle board K	0.167	0.167	0.167	[22]

References

[1] DIN Deutsches Institut für Normung e.V., EN 13377:2002 (D), Prefabricated timber formwork beams – Requirements, classification and assessment; German version, 2002.
[2] Dietsch P, Tannert T. Assessing the integrity of glued-laminated timber elements. Constr Build Mater 2015;101:1259–70. URL http://www.sciencedirect.com/science/article/pii/S0950061815300180.
[3] Eitelberger J, Hofstetter K, Dvinskikh S. A multi-scale approach for simulation of transient moisture transport processes in wood below the fiber saturation point. Compos Sci Technol 2011;71(15):1727–38. URL http://www.sciencedirect.com/science/article/pii/S0266353811002946.
[4] Svensson S, Turk G, Hozjan T. Predicting moisture state of timber members in a continuously varying climate. Eng Struct 2011;33(11):3064–70. URL http://www.sciencedirect.com/science/article/pii/S0141029611001908.
[5] Fortino S, Genoese A, Genoese A, Nunes L, Palma P. Numerical modelling of the hygro-thermal response of timber bridges during their service life: A monitoring case-study. Constr Build Mater 2013;47:1225–34. URL http://www.sciencedirect.com/science/article/pii/S0950061813005278.
[6] Fortino S, Hradil P, Metelli G. Moisture-induced stresses in large glulam beams. case study: Vihantasalmi bridge. Wood Mater Sci Eng 2019;14(5):366–80. https://doi.org/10.1080/17480272.2019.1638828.
[7] Fortino S, Hradil P, Genoese A, Genoese A, Pousette A. Numerical hygro-thermal analysis of coated wooden bridge members exposed to northern european climates. Constr Build Mater 2019;208:492–505. URL http://www.sciencedirect.com/science/article/pii/S0950061819304854.
[8] Autengruber M, Lukacevic M, Füssl J. Finite-element-based moisture transport model for wood including free water above the fiber saturation point. Int J Heat Mass Transf 2020;161:120228. URL http://www.sciencedirect.com/science/article/pii/S0017931020331641.
[9] Konopka D, Kaliske M. Transient multi-fickian hygro-mechanical analysis of wood. Comput Struct 2018;197:12–27. URL http://www.sciencedirect.com/science/article/pii/S0045794917310684.
[10] Fangtian D, Lipin C, Shufen Z. Determination of static and dynamic diffusion coefficients of moisture in particleboards. J Northeast Forestry Univ 1993;4(2):87–92. https://doi.org/10.1007/BF02843078.
[11] Sonderegger W, Niemz P. Thermal conductivity and water vapour transmission properties of wood-based materials. Eur J Wood Wood Prod 2009;67(3):313–21. https://doi.org/10.1007/s00107-008-0304-y.
[12] Lukacevic M, Füssl J, Lampert R. Failure mechanisms of clear wood identified at wood cell level by an approach based on the extended finite element method. Eng Fract Mech 2015;144:158–75. URL http://www.sciencedirect.com/science/article/pii/S001379441500332X.
[13] Lukacevic M, Füssl J. Application of a multisurface discrete crack model for clear wood taking into account the inherent microstructural characteristics of wood cells. Holzforschung 2016;70(9):845–53.
[14] Lukacevic M, Lederer W, Füssl J. A microstructure-based multisurface failure criterion for the description of brittle and ductile failure mechanisms of clear-wood. Eng Fract Mech 2017;176:83–99. URL http://www.sciencedirect.com/science/article/pii/S0013794416307603.
[15] Füssl J, Li M, Lukacevic M, Eberhardsteiner J, Martin CM. Comparison of unit cell-based computational methods for predicting the strength of wood. Eng Struct 2017;141:427–43. URL http://www.sciencedirect.com/science/article/pii/S0141029617307253.
[16] Li M, Füssl J, Lukacevic M, Eberhardsteiner J, Martin CM. Strength predictions of clear wood at multiple scales using numerical limit analysis approaches. Comput Struct 2018;196:200–16. URL http://www.sciencedirect.com/science/article/pii/S0045794917311550.
[17] Autengruber M, Lukacevic M, Gröstlinger C, Füssl J. Finite-element-based prediction of moisture-induced crack patterns for cross sections of solid wood and glued laminated timber exposed to a realistic climate condition. Constr Build Mater 2021;271:121775. URL http://www.sciencedirect.com/science/article/pii/S095006182033779X.
[18] Ehart RJA, Stanzl-Tschegg SE, Tschegg EK. Characterization of crack propagation in particleboard. Wood Sci Technol 1996;30(5):307–21. https://doi.org/10.1007/BF00223551.
[19] Krabbenhøft K, Damkilde L. A model for non-Fickian moisture transfer in wood. Mater Struct 2004;37(9):615–22. https://doi.org/10.1007/BF02483291.
[20] Whitaker S, Hartnett JP, Irvine TF. Simultaneous heat, mass, and momentum transfer in porous media: A theory of drying. In: Advances in Heat Transfer, vol. 13, Elsevier, 1977, p. 119–203. http://www.sciencedirect.com/science/article/pii/S0065271708702235.
[21] Documentation Abaqus. Abaqus Online Documentation. Providence, RI, USA: Dassault Systemes Simulia Corporation; 2016.
[22] DIN Deutsches Institut für Normung e.V., DIN EN ISO 10456:2010–05, Building materials and products – Hygrothermal properties – Tabulated design values and procedures for determining declared and design thermal values; German version, 5 2010.
[23] Volkmer T, Schmidt J-A, Kranitz K, Niemz P. Untersuchungen zum Einfluss der Klebstoffart auf den Diffusionswiderstand von Holzverklebungen. Bauphysik 2012;34(2):55–60. https://doi.org/10.1002/bapi.201200006.
[24] Niklewski J, Fredriksson M, Isaksson T. Moisture content prediction of rain-exposed wood: Test and evaluation of a simple numerical model for durability applications. Build Environ 2016;97:126–36. URL http://www.sciencedirect.com/science/article/pii/S0360132315301992.
[25] Hofstetter K, Hellmich C, Eberhardsteiner J. Development and experimental validation of a continuum micromechanics model for the elasticity of wood. Eur J Mech A Solids 2005;24(6):1030–53. URL http://www.sciencedirect.com/science/article/pii/S0997753805000963.
[26] Hofstetter K, Hellmich C, Eberhardsteiner J. Micromechanical modeling of solid-type and plate-type deformation patterns within softwood materials. A review and an improved approach. Holzforschung 2007;61(4):343–51. https://doi.org/10.1515/HF.2007.058.
[27] Gloimüller S, De Borst K, Bader T, Eberhardsteiner J. Determination of the linear elastic stiffness and hygroexpansion of softwood by a multilayered unit cell using poromechanics. Interact Multiscale Mech 2012;5(3):229–65.
[28] Tsai SW, Wu EM. A general theory of strength for anisotropic materials. J Compos Mater 1971;5(1):58–80. https://doi.org/10.1177/002199837100500106.
[29] Pech S, Lukacevic M, Füssl J. A robust multisurface return-mapping algorithm and its implementation in abaqus. Finite Elem Anal Des 2021;190:103531. URL https://www.sciencedirect.com/science/article/pii/S0168874X21000159.
[30] Gerhards C. Effect of moisture content and temperature on the mechanical properties of wood: an analysis of immediate effects. Wood Fiber 1982;14(1):4–36.
[31] Fink G. Influence of varying material properties on the load-bearing capacity of glued laminated timber, Ph.D. thesis, ETH Zurich, 2014.
[32] Fink G, Frangi A, Kohler J. Probabilistic approach for modelling the load-bearing capacity of glued laminated timber. Eng Struct 2015;100:751–62. URL https://www.sciencedirect.com/science/article/pii/S0141029615003910.
[33] DIN Deutsches Institut für Normung e.V., DIN EN 312:2010-12, Particleboards – Specifications; German version, 12 2010.
[34] Bader TK, Dastoorian F, Ebrahimi G, Unger G, Lahayne O, Hellmich C, Pichler B. Combined ultrasonic-mechanical characterization of orthotropic elastic properties of an unrefined bagasse fiber-polypropylene composite. Compos Part B: Eng 2016;95:96–104. URL http://www.sciencedirect.com/science/article/pii/S1359836816301585.
[35] Pavlekovics A, Niemz P, Sonderegger W, Molnar S. Studies on the influence of wood moisture content on selected properties of particle boards and MDF. Holz als Roh- und Werkstoff 2008;66(2):99–105. https://doi.org/10.1007/s00107-007-0199-z.
[36] DIN Deutsches Institut für Normung e.V., DIN EN 12369-1:2001-04, Wood-based panels – Characteristic values for structural design – Part 1: OSB, particleboards and fibreboards; German version, 4 2001.
[37] Sonderegger W, Niemz P. Investigation of swelling and thermal expansion of fibreboard, particleboard and plywood. Holz als Roh- und Werkstoff 2005;64(1):11–20. https://doi.org/10.1007/s00107-005-0043-2.
[38] Holzforschung-Austria, Radikale Schalungsinnovationen Projektteil SSTH - Stärkerer Systemträger Holz Pilzresistenz und Feuchteverhalten, Tech. rep., Holzforschung-Austria, 2010.
[39] Frandsen HL. Selected constitutive models for simulating the hygromechanical response of wood. Ph.D. thesis. Aalborg University; 2007.
[40] Siau J. Transport Processes in Wood. Berlin Heidelberg New York Tokyo: Springer-Verlag; 1984. https://doi.org/10.1007/978-3-642-69213-0.
[41] Schirmer R. Die Diffusionszahl von Wasserdampf-Luft-Gemischen und die Verdampfungsgeschwindigkeit. VDI Beiheft Verfahrenstechnik 1938;1938(6):170–7.
[42] Frandsen HL, Damkilde L, Svensson S. A revised multi-Fickian moisture transport model to describe non-Fickian effects in wood. Holzforschung 2007;61:563–572. URL http://www.degruyter.com/view/j/hfsg.2007.61.issue-5/hf.2007.085/hf.2007.085.xml.
[43] Kollmann F. Technologie des Holzes und der Holzwerkstoffe - Band 1. Berlin Heidelberg: Springer-Verlag; 1951.
[44] Perré P, Turner IW. A 3-d version of transpore: a comprehensive heat and mass transfer computational model for simulating the drying of porous media. Int J Heat Mass Transf 1999;42(24):4501–21. URL http://www.sciencedirect.com/science/article/pii/S0017931099000988.

[45] Yang Q-X. Study on the specific heat of wood by statistical mechanics. J Forest Res 2000;11(4):265–8. https://doi.org/10.1007/BF02844975.
[46] Eitelberger J. A multiscale material description for wood below the fiber saturation point with particular emphasis on wood-water interactions, Ph.D. thesis, Wien, Techn. Univ., Diss., 2011 (2011). https://permalink.catalogplus.tuwien.at/AC07811592.
[47] Skaar C. Wood-Water Relations. Berlin Heidelberg: Springer-Verlag; 1988. https://doi.org/10.1007/978-3-642-73683-4.
[48] Stanish MA, Schajer GS, Kayihan F. A mathematical model of drying for hygroscopic porous media. AIChE J 1986;32(8):1301–11. https://doi.org/10.1002/aic.690320808.
[49] Turner IW. A two-dimensional orthotropic model for simulating wood drying processes. Appl Math Model 1996;20(1):60–81. URL http://www.sciencedirect.com/science/article/pii/0307904X9500106T.
[50] Perré P, Moser M, Martin M. Advances in transport phenomena during convective drying with superheated steam and moist air. Int J Heat Mass Transf 1993;36(11):2725–46. URL http://www.sciencedirect.com/science/article/pii/001793109390093L.